

BESIII Analysis Memo

DocDB-817

BAM-817

September 22, 2019

Amplitude Analysis and Branching Fraction Measurement of

$$D_s^+ \rightarrow K^+ K^- \pi^+$$

Meng Wang^a, Yu Lu^a, and Liaoyuan Dong^a, and Huaimin Liu^a

^a*Institute of High Energy Physics, CAS*

Internal Referee Committee

Ref1 xx (Chair)^d, Ref2 xx^e, and Ref3 xx^f

^d*Department of Computer Science and Engineering*

^e*Department of Electrical Engineering*

^f*Latex Univeristy*

DocDB : <http://docbes3.ihep.ac.cn/cgi-bin/DocDB/ShowDocument?docid=817>

Hypernews : <http://hnb3.ihep.ac.cn/HyperNews/get/paper817.html>

Abstract

We report the amplitude analysis and branching fraction measurement of $D_s^+ \rightarrow K^+ K^- \pi^+$ decay using a data sample of 3.19 fb^{-1} recorded with BESIII detector at a center-of-mass energy of 4.178 GeV. We perform a model-independent partial wave analysis (MIPWA) in the low $K^+ K^-$ region to extract the $K^+ K^-$ S -wave lineshape. We also perform an amplitude analysis on a nearly background free sample of 4399 events to investigate the substructure, and determine the relative fractions and the phases among the different intermediate processes. The amplitude analysis results provide an accurate detection efficiency and allow measurement of the branching fraction of $D_s^+ \rightarrow K^+ K^- \pi^+$ to be $\mathcal{B}(D_s^+ \rightarrow K^+ K^- \pi^+) = (5.47 \pm 0.07_{\text{stat.}} \pm 0.13_{\text{sys.}})\%$.

Contents

1	1 Introduction	3
1.1	The Scalar Mesons $f_0(980)$ and $a_0(980)$	3
1.2	The Dynamics of the Strong Interaction	4
1.3	Amplitude Analysis	4
2	Data Set and Monte Carlo Samples	7
3	Event Selection	8
3.1	Tracking, PID, π^0 , η , η' and K_S^0 Reconstruction	8
3.2	D_s Selection	9
3.3	Signal Selection	10
4	Partial Wave Analysis in the Low K^+K^- Mass Region	11
4.1	Event Selection	11
4.2	Background Analysis	11
4.3	Partial Wave Analysis	16
4.4	S-wave Parameterization at the K^+K^- Threshold	17
4.5	Systematic Uncertainties	19
5	Amplitude Analysis	22
5.1	Event Selection	22
5.2	Background Analysis	22
5.3	Fit Method	23
5.3.1	Propagator	25
5.3.2	Blatt-Weisskopf Barriers	26
5.3.3	Spin Factors	26
5.4	Fit Fraction	26
5.5	Fit Result	27
5.6	Systematic Uncertainties	30
6	Branching Fraction Measurements	34
6.1	Event Selection	34
6.2	Analytic Strategy	34
6.3	Results of Branching Fraction	37

1	6.4 Systematic Uncertainties	37
2	7 Summary	40
3	A The attemption to distinguish $a_0(980)$ and $f_0(980)$	44

1 Introduction

The Cabibbo-favored (CF) $D_s^+ \rightarrow K^+ K^- \pi^+$ decay has a large branching fraction and low background contamination. This decay is, therefore, usually suited as a reference channel for other decays of the D_s meson and used as normalization for decay chains involving charm quarks. An accurate knowledge of its substructure is important to reduce systematic uncertainties in analyses using this channel. The study of intermediate processes in this decay can also illuminates light meson spectroscopy and shed light on different production mechanisms.

1.1 The Scalar Mesons $f_0(980)$ and $a_0(980)$

The Constituent Quark Model has been very successful in the past few decades by explaining how hadrons are made up. Based on this model, the nonets of pseudo-scalar, vector, and tensor mesons are now well identified. However, the identification of the scalar mesons is still uncertain due to the broad widths and the lack of a distinctive angular distribution. Among the candidates for the spin-parity $J^{PC} = 0^{++}$ nonet, the parameters of some states such as $f_0(980)$ and $a_0(980)$ are not well measured,

Recently, the decay $D_s^+ \rightarrow a_0(980)^0 \pi^+$ has been observed through $D_s^+ \rightarrow \pi^+ \pi^0 \eta$ [1]. The overlap of $f_0(980)$ and $a_0(980)$ make it very difficult to distinguish them (Appendix A). From the Dalitz plot analysis of $D_s^+ \rightarrow \pi^+ \pi^- \pi^+$, we can get the branching fraction $\mathcal{B}(D_s^+ \rightarrow f_0(980) \pi^+, f_0(980) \rightarrow \pi^+ \pi^-)$. With the branching ratio of $\Gamma_{f_0(980)}(K^+ K^-)/\Gamma_{f_0(980)}(\pi^+ \pi^-)$, we can obtain:

$$\mathcal{B}(D_s^+ \rightarrow f_0(980) \pi^+, f_0(980) \rightarrow K^+ K^-) = \mathcal{B}(D_s^+ \rightarrow f_0(980) \pi^+, f_0(980) \rightarrow \pi^+ \pi^-) \frac{\Gamma_{f_0(980)}(K^+ K^-)}{\Gamma_{f_0(980)}(\pi^+ \pi^-)}. \quad (1)$$

In a similar way, we can obtain:

$$\mathcal{B}(D_s^+ \rightarrow a_0(980) \pi^+, a_0(980) \rightarrow K^+ K^-) = \mathcal{B}(D_s^+ \rightarrow a_0(980) \pi^+, a_0(980) \rightarrow \pi^0 \eta) \frac{\Gamma_{a_0(980)}(K^+ K^-)}{\Gamma_{a_0(980)}(\pi^0 \eta)}. \quad (2)$$

So the ratio of fit fractions between \mathcal{R} of $D_s^+ \rightarrow f_0(980) \pi^+$ and $D_s^+ \rightarrow a_0(980) \pi^+$ is:

$$\mathcal{R} = \frac{\mathcal{B}(D_s^+ \rightarrow f_0(980) \pi^+, f_0(980) \rightarrow \pi^+ \pi^-) \frac{\Gamma_{f_0(980)}(K^+ K^-)}{\Gamma_{f_0(980)}(\pi^+ \pi^-)}}{\mathcal{B}(D_s^+ \rightarrow a_0(980) \pi^+, a_0(980) \rightarrow \pi^0 \eta) \frac{\Gamma_{a_0(980)}(K^+ K^-)}{\Gamma_{a_0(980)}(\pi^0 \eta)}}. \quad (3)$$

The confirmation of the value \mathcal{R} in Eq. 3 can help to fix the ratio in amplitude analyses and then distinguish $f_0(980)$ and $a_0(980)$ at the low end of $K^+ K^-$ mass spectrum. Using isospin relations, the relation between $\Gamma_{f_0(980)}(\pi\pi)/\Gamma_{f_0(980)}(\pi\pi + K\bar{K})$ and $\Gamma_{f_0(980)}(K^+ K^-)/\Gamma_{f_0(980)}(\pi^+ \pi^-)$ is:

$$\frac{\Gamma_{f_0(980)}(K^+ K^-)}{\Gamma_{f_0(980)}(\pi^+ \pi^-)} = \frac{3}{4} \cdot \left[\frac{1}{\frac{\Gamma_{f_0(980)}(\pi\pi)}{\Gamma_{f_0(980)}(\pi\pi) + \Gamma_{f_0(980)}(K\bar{K})}} - 1 \right]. \quad (4)$$

1 However, the value of $\Gamma_{f_0(980)}(K^+K^-)/\Gamma_{f_0(980)}(\pi^+\pi^-)$ is not well measured, shown in Table 1. $f_0(980)$ is
 2 very close to $K\bar{K}$ threshold and has strong coupling to $\pi\pi$ and $K\bar{K}$ final states. So, in this analysis, we use
 3 $S(980)$ to denote the $a_0(980)$ and $f_0(980)$ resonances in Sec. 5. And we perform a model-independent
 4 partial wave analysis (MIPWA) to extract the $S(980)$ lineshape in the low end of K^+K^- mass spectrum
 5 (Sec. 4).

Table 1: The $f_0(980)$ branching ratio $\Gamma_{f_0(980)}(\pi\pi)/[\Gamma_{f_0(980)}(\pi\pi) + \Gamma_{f_0(980)}(K\bar{K})]$

value	Collaboration	comment
0.52 ± 0.12	BABAR	$B^\pm \rightarrow K^\pm \pi^\pm \pi^\mp$ [2]
$0.75^{+0.11}_{-0.13}$	BESII	$\chi_{c0} \rightarrow 2\pi^+ 2\pi^-, \pi^+ \pi^- K^+ K^-$ [3]
0.84 ± 0.02	SPEC	Combined fit [4]

6 1.2 The Dynamics of the Strong Interaction

7 Hadronic decays of charmed mesons are important for understanding the dynamics of the strong
 8 interaction in the low energy regime. Fig. 1 illustrates main Feynman diagrams related to the $D_s^+ \rightarrow$
 9 $K^+ K^- \pi^+$ decay. Experimental measurements can help to refine theoretical models [5]. Table 2 shows the
 predictions of the branching fractions of $D_s^+ \rightarrow \bar{K}^*(892)^0 K^+$ and $D_s^+ \rightarrow \phi(1020)\pi^+$.

Table 2: $\mathcal{B}(A1)$, $\mathcal{B}(S4)$, $\mathcal{B}(pole)$ and $\mathcal{B}(FAT[mix])$ are 4 theory predictions [5].

Mode	$\mathcal{B}(A1)$ (%)	$\mathcal{B}(S4)$ (%)	$\mathcal{B}(pole)$ (%)	$\mathcal{B}(FAT[mix])$ (%)
$D_s^+ \rightarrow \bar{K}^*(892)^0 K^+$	3.92 ± 1.13	3.93 ± 1.10	4.2 ± 1.7	4.07
$D_s^+ \rightarrow \phi(1020)\pi^+$	4.49 ± 0.40	4.51 ± 0.43	4.3 ± 0.6	3.4

10

11 1.3 Amplitude Analysis

12 Knowledge of the substructure in $D_s^+ \rightarrow K^+ K^- \pi^+$ decay allows us to properly determine the detection
 13 efficiency when measuring its branching fraction. Dalitz plot analyses of this decay have been performed
 14 by the E687 [6], CLEO [7] and Babar [8] collaborations. E687 used about 700 events and did not take
 15 $f_0(1370)\pi^+$ into account. For CLEO-c, about 14400 events with purity about 84.9% were selected with
 16 the single tag method. The analysis of BABAR used about 100000 events with purity about 95%.
 17 Table 3 shows the comparison of the fitted decay fractions with the Dalitz plot analyses of previous
 18 analyses.

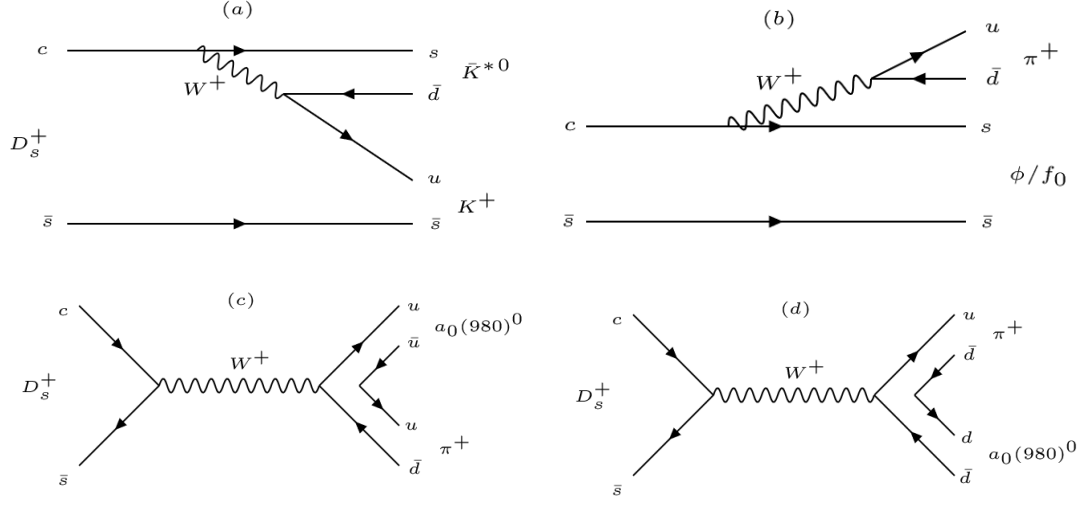


Figure 1: Main decay diagrams associated with $D_s^+ \rightarrow K^+ K^- \pi^+$ decay. The main contribution comes from the tree diagram with an internal W^+ emission (Fig. 1(a)), that describes the $D_s^+ \rightarrow \bar{K}^*(892)^0 K^+$ decay, the diagram with an external W^+ emission (Fig. 1(b)), that describes the diagram $D_s^+ \rightarrow \phi \pi^+ / f_0 \pi^+$, and the diagram with W-annihilation (Fig. 1(c) and Fig. 1(d)), that describes the decay $D_s \rightarrow a_0(980)^0 \pi^+$.

Table 3: Comparison between Babar, CLEO-c and E687 Dalitz plot analysis.

Decay mode	Fit fraction(BABAR)	Fit fraction(CLEO-c)	Fit fraction(E687)
$D_s^+ \rightarrow \bar{K}^*(892)^0 K^+$	$47.9 \pm 0.5 \pm 0.5$	$47.4 \pm 1.5 \pm 0.4$	$47.8 \pm 4.6 \pm 4.0$
$D_s^+ \rightarrow \phi(1020) \pi^+$	$41.4 \pm 0.8 \pm 0.5$	$42.2 \pm 1.6 \pm 0.3$	$39.6 \pm 3.3 \pm 4.7$
$D_s^+ \rightarrow S(980) \pi^+$	$16.4 \pm 0.7 \pm 2.0$	$28.2 \pm 1.9 \pm 1.8$	$11.0 \pm 3.5 \pm 2.6$
$D_s^+ \rightarrow \bar{K}_0^*(1430)^0 K^+$	$2.4 \pm 0.3 \pm 1.0$	$3.9 \pm 0.5 \pm 0.5$	$9.3 \pm 3.2 \pm 3.2$
$D_s^+ \rightarrow f_0(1710) \pi^+$	$1.1 \pm 0.1 \pm 0.1$	$3.4 \pm 0.5 \pm 0.3$	$3.4 \pm 2.3 \pm 3.5$
$D_s^+ \rightarrow f_0(1370) \pi^+$	$1.1 \pm 0.1 \pm 0.2$	$4.3 \pm 0.6 \pm 0.5$...
$\sum FF(\%)$	$110.2 \pm 0.6 \pm 2.0$	$129.5 \pm 4.4 \pm 2.0$	111.1
χ^2/NDF	$\frac{2843}{2305-14} = 1.2$	$\frac{178}{117} = 1.5$	$\frac{50.2}{33} = 1.5$
Events	96307 ± 369	12226 ± 22	701 ± 36

1 From Table 3, we can see an obvious difference of decay fraction of $S(980)\pi^+$ between BABAR and
2 CLEO-c. In this analysis with the double tag method, we can get a nearly background free data sample,
3 which is good to perform the amplitude analysis.

2 Data Set and Monte Carlo Samples

We use 3.195 fb^{-1} data set collected at $E_{cm} = 4.178 \text{ GeV}$ by BESIII detector in 2016. Both data sample and Monte Carlo samples are reconstructed under BOSS7.0.3. All samples were generated with run-dependent E_{cm} [10], except for the Bhabha, μ -pair and Two-photon fusion events. For these three types of events, we used a constant E_{cm} at 4178.37 MeV, which is twice of a luminosity-weighted average of the measured beam energy in the center-of-mass frame. Total 40 rounds of generic MC with each round equaling to data size are used for background study, tag efficiencies estimation (rounds 01-30) and input-output check for branching fraction measurement (rounds 31-40). They are available at /besfs3/offline/data/703-1/4180/mc/. For each round of generic MC, the detail components and corresponding size of each Monte Carlo sample are given in Table 4.

Table 4: Component and corresponding sizes, assume luminosity = 3195/pb.

Component	cross section (pb)	Size (M)	directory
$D^0 D^0$	179	0.5719	D0D0
$D^+ D^-$	197	0.6294	DpDm
$D^{*0} D^0$	1211	3.8691	DST0D0
$D^{*+} D^-$	1296	4.1407	DSTpDm
$D^{*0} D^{*0}$	2173	6.9427	DST0DST0
$D^{*+} D^{*-}$	2145	6.8533	DSTpDSTm
$D_s^+ D_s^-$	7	0.0225	DsDs
$D_s^{*+} D_s^-$	961	3.0700	DsSTDs
$DD^* \pi^+$	383	1.2237	DDSTPIp
$DD^* \pi^0$	192	0.6134	DDSTPI0
$DD \pi^+$	50	0.1598	DDPIp
$DD \pi^0$	25	0.0799	DDPI0
Component	cross section (nb)	Size (M)	directory
$q\bar{q}$	13.8	44.0910	qq
$\gamma J/\psi$	0.40	1.2780	RR1S
$\gamma \psi(2S)$	0.42	1.3419	RR2S
$\gamma \psi(3770)$	0.06	0.1917	RR3770
$\tau\tau$	3.45	11.0228	tt
$\mu\mu$	5.24	16.7418	mm
ee	423.99	13.5465(0.01 \times)	ee
Two-photon fusion	1.7	5.4315	TwoGam
HCT	0.10178	0.3252	HCT

For the Signal MC, we generate the signal events with one D_s decaying to signal mode using the generator “DIY”, in which the parameters are obtained from the fit to data. phase space (PHSP) MC and Signal MC are used in MC integration required for the amplitude fit. The Signal MC is also used in the input/output check.

3 Event Selection

At $E_{cm} = 4.178$ GeV, pairs of $D_s D_s^*$ are produced, and the D_s^* decays to either $D_s \gamma$ or $D_s \pi^0$. So the D_s^* mesons are produced in pairs without additional charged hadrons ($K^\pm(\pi^\pm)$). We do not search for the gamma or π^0 from the D_s decay. These unique $D_s^+ D_s^-$ final states provide us an opportunity to employ the double tag method to measure the absolute branching fractions of D_s meson decays. The double tag method also provide clean samples to perform an amplitude analysis.

3.1 Tracking, PID, π^0 , η , η' and K_S^0 Reconstruction

D_s candidates are built from K^\pm , π^\pm , π^0 , η , η' and K_S^0 . The selections of the particles to build D_s candidates are performed with DTagAlg-00-01-05 package with the default setting, which are summarized below.

- Tracking:

- The properties of charged tracks are determined based on the MDC information. Charged track candidates must satisfy:

- $|\cos\theta| < 0.93$,

- $|dr| < 1$ cm and $|dz| < 10$ cm,

where $|dr|$ and $|dz|$ are defined as the one reconstructed minus the interaction point.

- Particle ID:

- Charged tracks are identified as pions or kaons with Particle Identification (PID), which is implemented by combing the information of the energy loss (dE/dx) in MDC and the time-of-flight measured from the TOF system. Kaon and Pion are identified with the requirements that

- $Prob(K) > 0$ and $Prob(K) > Prob(\pi)$ for K ,

- $Prob(\pi) > 0$ and $Prob(\pi) > Prob(K)$ for π , where $Prob(X)$ is the probability of hypothesis X, X can be π or K .

- π^0/η selection: π^0/η candidates are reconstructed through $\pi^0 \rightarrow \gamma\gamma$ ($\eta \rightarrow \gamma\gamma$) with package of PioEtaToGGRecAlg.

The photons are reconstructed as energy showers on the EMC. We require:

- Minimum energy for barrel showers ($|\cos\theta| < 0.8$): $E_{min} > 25$ MeV/ c^2 ,

- Minimum energy for endcap showers ($0.86 < |\cos\theta| < 0.92$): $E_{min} > 50 \text{ MeV}/c^2$,
- Shower within other $|\cos\theta|$ regions are rejected,
- The shower time is required to be within 700 ns of the event start time to suppress the electronics noise.

Then we perform a constrained fit on the photon pairs to the nominal π^0/η mass and require:

- The unconstrained invariant mass for π^0 : $0.115 < M(\gamma\gamma) < 0.015 \text{ GeV}/c^2$,
 - The unconstrained invariant mass for η : $0.490 < M(\eta) < 0.580 \text{ GeV}/c^2$,
 - Mass fit: $\chi^2_{1c} < 30$.
- η' selection: The η' candidates are reconstructed with $\pi^+\pi^-\eta$, the invariant mass for $\pi^+\pi^-\eta$ is required to fall into the range of $[0.938, 0.978] \text{ GeV}/c^2$.
 - K_S^0 selection: K_S^0 candidates are reconstructed using VeeVertexAlg package with two opposite charged tracks with requiring:
 - $|\cos\theta| < 0.93$,
 - $|dz| < 20 \text{ cm}$.

For each pair of tracks, a constrained vertex fit is performed and the track parameters' results are used to get the invariant mass $M(K_S^0)$. Then the decay length of K_S^0 is obtained with second vertex fit by the SecondVertexFit package. For K_S^0 selection, we require:

- $0.487 \text{ GeV}/c^2 < M(K_S^0) < 0.511 \text{ GeV}/c^2$,
- Significance of the K_S^0 decay length has two standard deviations.

3.2 D_s Selection

The D_s candidates are constructed from individual π , K, η , η' , K_S^0 and π^0 in an event. The D_s candidates fall into the mass window of $1.87 < m_{D_s} < 2.06 \text{ GeV}/c^2$ and the corresponding M_{rec} satisfied $2.051 < M_{rec} < 2.180 \text{ GeV}/c^2$ are retained for further study. The definition of M_{rec} is

$$M_{rec} = \sqrt{(E_{cm} - \sqrt{p_{D_s}^2 + m_{D_s}^2})^2 - |\vec{p}_{cm} - \vec{p}_{D_s}|^2}, \quad (5)$$

where E_{cm} is the energy of initial state calculated from the beam energy [10], \vec{p}_{D_s} is the momentum of D_s candidate, m_{D_s} is D_s mass quoted from PDG [11], and \vec{p}_{cm} and \vec{p}_{D_s} are four-momentum of the initial state and the decay products of the D_s candidate, respectively.

1 **3.3 Signal Selection**

2 We use different methods to select events in the model independent analysis (Sec. [4.1](#)), the amplitude
3 analysis (Sec. [5.1](#)) and the branching fraction measurement (Sec. [6.1](#)).

4 Partial Wave Analysis in the Low K^+K^- Mass Region

In the K^+K^- threshold, both $a_0(980)$ and $f_0(980)$ can be present, and both resonances have very similar parameters which suffer from large uncertainties. In this section we obtain the model-independent information on the K^+K^-S wave by performing a partial wave analysis (PWA) in the K^+K^- threshold region.

4.1 Event Selection

After the selection in Sec. 3, we select signals for the model independent partial wave analysis. To retain enough statistics, we decide to use the single-tag method, and only to fully reconstruct one $D_s^+ \rightarrow K^+K^-\pi^+$ in each event. We veto the candidates with π^\pm (π^0) whose momentum is less than 0.1 GeV to remove soft π^\pm (π^0) from D^* decays. For each D_s candidate, all daughter tracks are added to apply a 1C kinematic fit constraining the mass of D_s . Then we select the best candidate with minimum χ_{1c}^2 .

4.2 Background Analysis

In order to suppress the background, the multiple-variable analysis (MVA) is used. We train MVA separately with different sets of variables for the two event categories depending on the D_s^+ origin. Sideband region used below is defined as the region of $1.90 < M(D_s) < 1.95 \text{ GeV}/c^2$ and $1.986 < M(D_s) < 2.03 \text{ GeV}/c^2$, where $M(D_s)$ is the invariant mass of D_s , and the signal region is $1.95 < M(D_s) < 1.986 \text{ GeV}/c^2$. Two categories of events are selected in a $M_{rec} - \Delta M$ 2D plane as shown in Fig. 2.

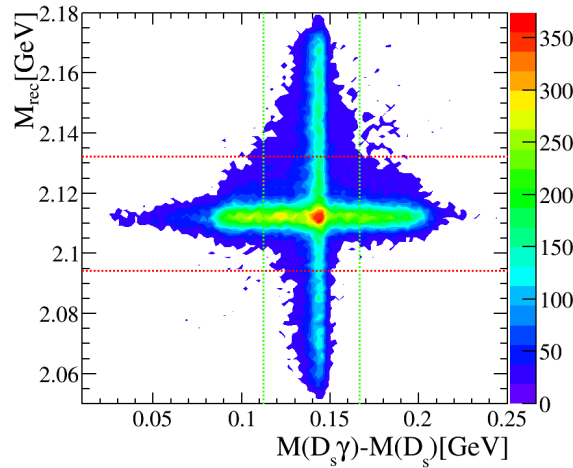


Figure 2: Two dimensional plane of M_{rec} versus $\Delta M \equiv M(D_s^+\gamma) - M(D_s^+)$ from the simulated $D_s^+ \rightarrow K^+K^-\pi^+$ decays. The red (green) dashed lines mark the mass window for the D_s^+ Cat. #0 (Cat. #1) around the M_{rec} (ΔM) peak.

- Cat. #0: Direct D_s^+ . We use the following variables whose distributions for signal and background are shown in Fig. 3 for generic MC and Fig. 4 for data,

1. M_{rec} ,
2. P_{rest} , defined as the total momentum of the tracks and neutrals in the rest of event (not part of the $D_s^+ \rightarrow K^+ K^- \pi^+$ candidate),
3. E_γ , defined as the energy of gamma from D_s^* .

From Fig. 3 and Fig. 4, we can see that the corresponding distributions of these variables of data and generic MC are roughly consistent.

- Cat. #1: Indirect D_s^+ . We use the following variables whose distributions for signal and background are shown in Fig. 5 for generic MC and Fig. 6 for data,

1. ΔM ,
2. M'_{rec} , defined as $M'_{rec} = \sqrt{(E_{cm} - \sqrt{p_{D_s\gamma}^2 + m_{D_s^*}^2})^2 - p_{D_s\gamma}^2}$, with $p_{D_s\gamma}$ as the momentum of the $D_s\gamma$ combination, $m_{D_s^*}$ as the nominal D_s^* mass,
3. N_{tracks} , defined as the total number of tracks and neutrals in an event.

From Fig. 5 and Fig. 6, we can see that the corresponding distributions of these variables of data and generic MC are roughly consistent.

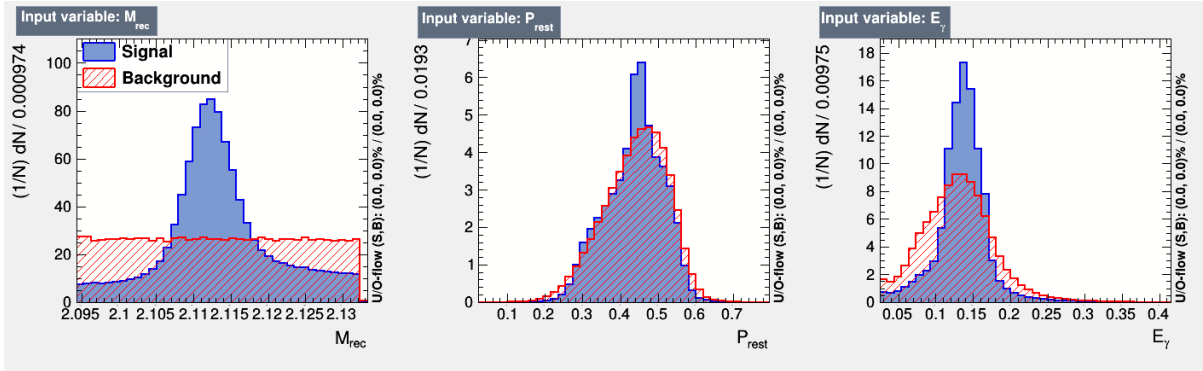


Figure 3: For event Cat. #0, distributions of MVA variables from simulated signal decays and background events.

As the results shown in Fig. 7, BDTG training and test samples are well matched. For event Cat. #0 (Cat. #1), the sample with BDTG value larger than 0.33 (0.65) is retained for further study. With the BDTG cut criteria, we can get a relatively pure sample (background less than 4%) and the background ratios of Cat. #0 and Cat. #1 are almost the same.

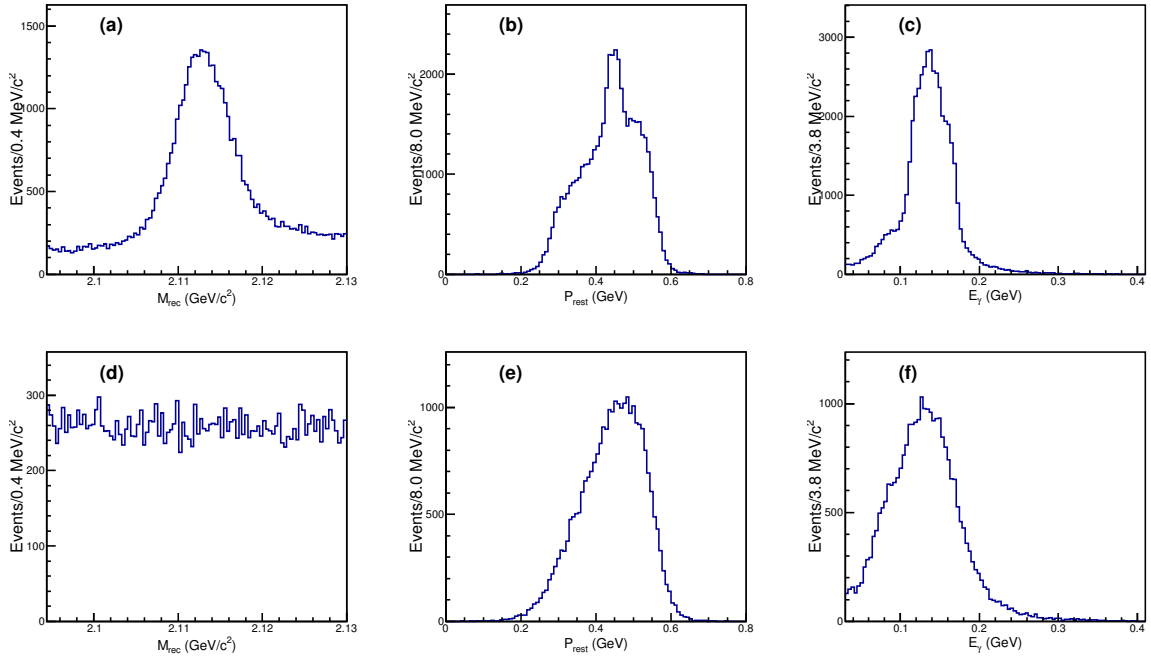


Figure 4: The distributions (Cat. #0) of these three observables ((a) and (d)) M_{rec} , ((b) and (e)) P_{rest} and ((c) and (f)) E_γ for ((a), (b) and (c)) signal and ((d), (e) and (f)) sideband regions of data.

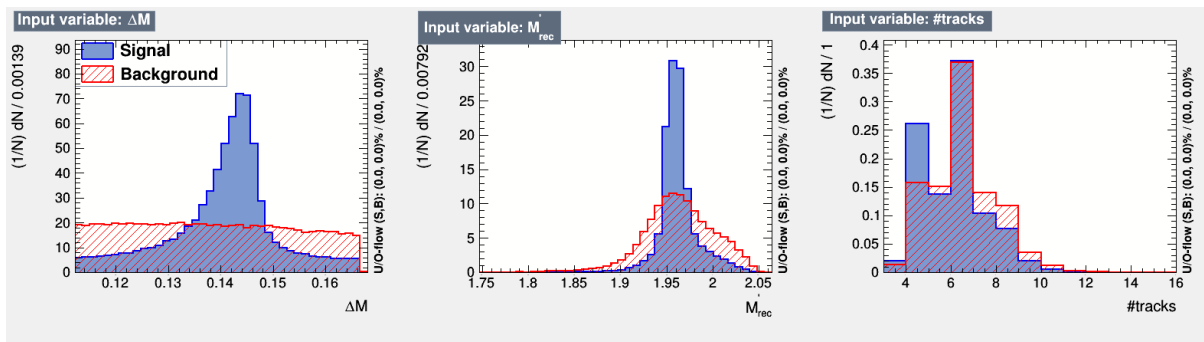


Figure 5: For event Cat. #1, distributions of MVA variables from simulated signal decays and background events.

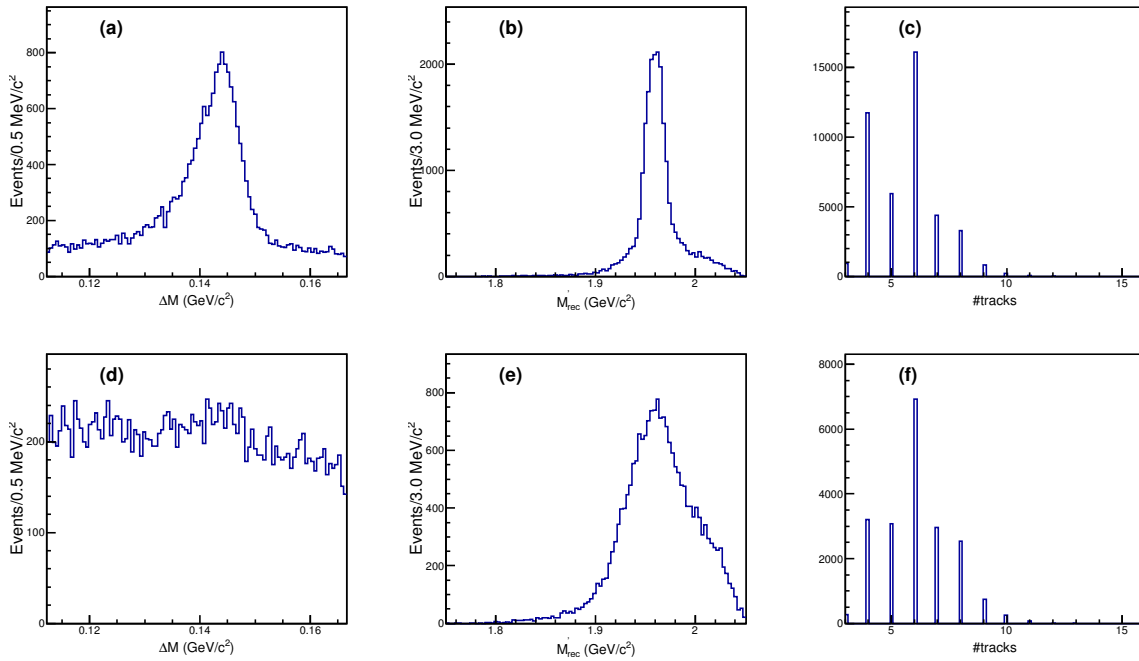


Figure 6: The distributions (Cat. #1) of these three observables ((a) and (d)) M_{rec} , ((b) and (e)) P_{rest} and ((c) and (f)) E_γ for ((a), (b) and (c)) signal and ((d), (e) and (f)) sideband regions from data.

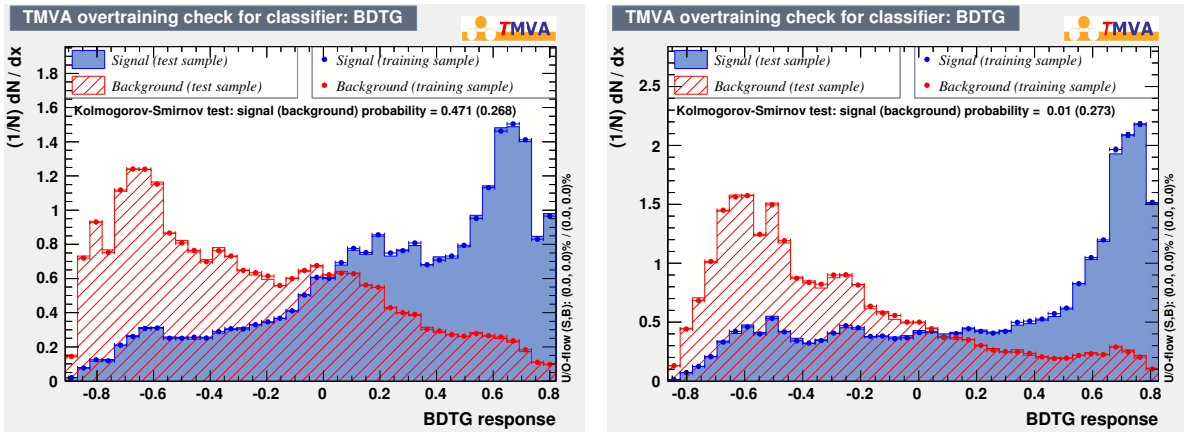


Figure 7: The comparisons between the training and test samples. The plot at left (right) is the comparison of Cat. #0 (Cat. #1).

After applying the BDTG requirement, the background shows no obviously peak around the region of $[1.95, 1.986] \text{ GeV}/c^2$ (Signal region), which are shown in Fig. 8. The fit to the signal D_s invariant mass gives the background yield in Signal region is 735.7 ± 30.0 , shown as in Fig. 9. In the fit, the signal shape is the MC shape convoluted with a Gaussian function and the background is described with second-order Chebychev polynomial.

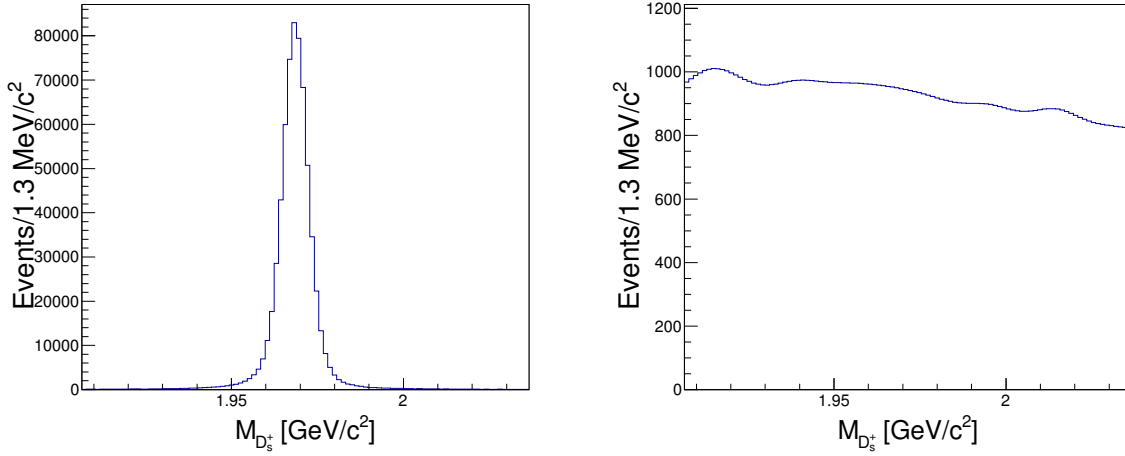


Figure 8: The signal and background distributions from generic MC after BDTG requirement.

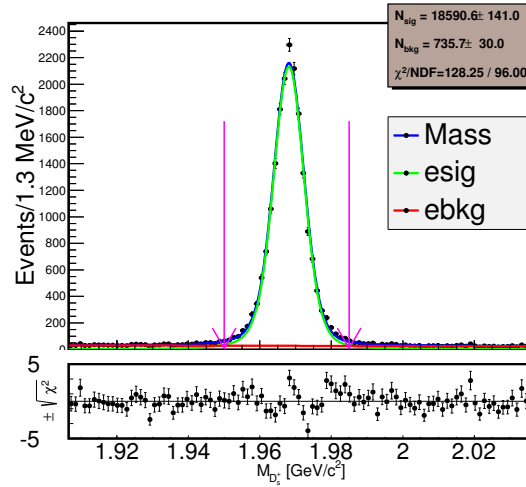


Figure 9: The fit to the signal D_s invariant mass (M_{D_s}) spectrum (the dots with error bars) after BDTG requirement, the area between the pink arrows is the signal area of the sample for MIPWA. The signal shape (green line) is the MC shape convoluted with a Gaussian function and the background shape (red line) is second-order Chebychev polynomial.

The projections of the “sideband” ($1.90 < M(D_s) < 1.95 \text{ GeV}/c^2$ and $1.986 < M(D_s) < 2.03 \text{ GeV}/c^2$) from data and generic MC with signal events removed are shown in Fig. 10. The corresponding plots agree well. Thus the generic MC sample with signal events removed is used to subtract the

1 background in data.

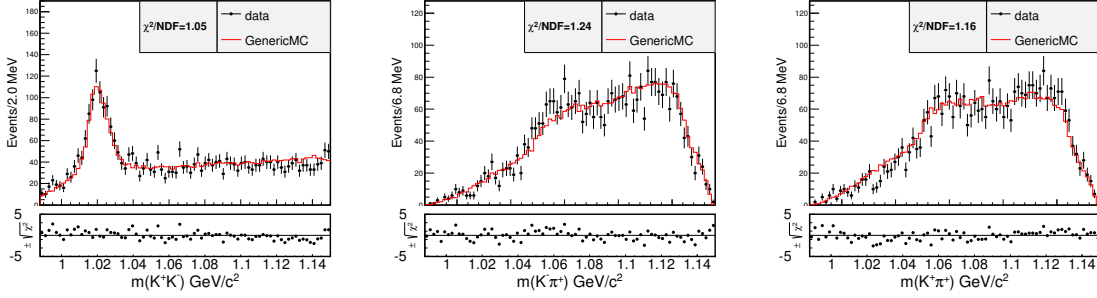


Figure 10: The projections of $m(K^+K^-)$, $m(K^-\pi^+)$, $m(K^+\pi^+)$ from “Sideband” for data (dots with error bars) and generic MC with signal events removed (red histogram) after BDTG requirement.

2 Figure 11 shows the shape comparison between data and MC for the inputs and outputs of BDTG.
 3 We can see that there is no significant difference. The background has been subtracted using the corresponding shape of “Sideband” in this shape comparison.

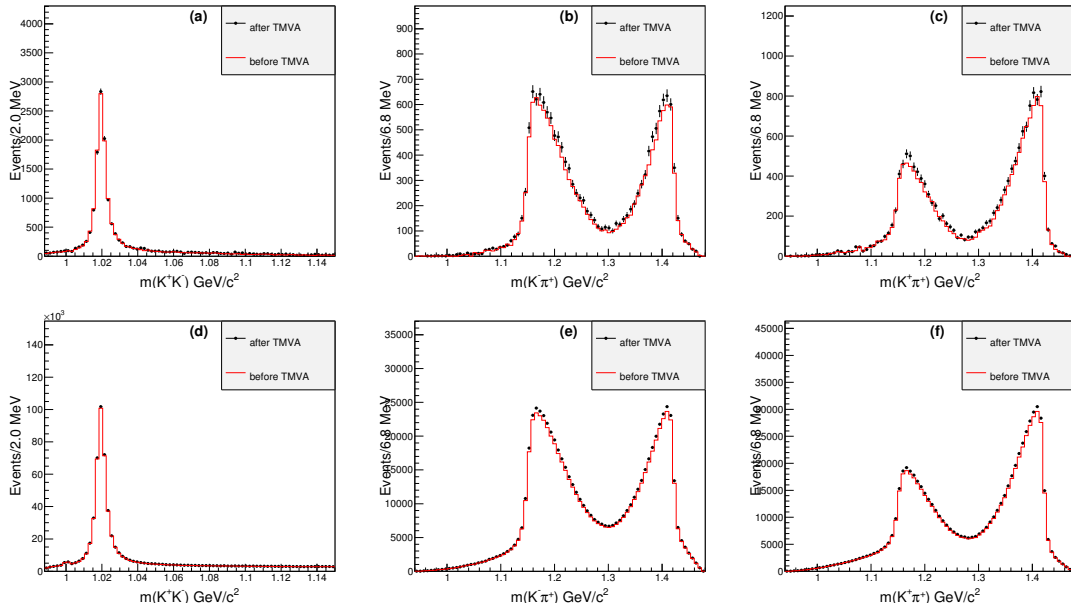


Figure 11: The shape comparison between data and MC for the inputs and outputs of BDTG. The background has been subtracted.

4

5 4.3 Partial Wave Analysis

6 Assuming N is the number of events for a given mass interval $I = [m_{K^+K^-}; m_{K^+K^-} + dm_{K^+K^-}]$, we
 7 write the corresponding angular distributions in terms of the appropriate spherical harmonic functions is

1 written

$$\frac{dN}{d \cos \theta} = 2\pi \sum_{k=0}^L \langle Y_k^0 \rangle Y_k^0(\cos \theta), \quad (6)$$

2 where $L = 2\ell_{max}$, and ℓ_{max} is the maximum orbital angular momentum quantum number required to
 3 describe the K^+K^- system at $m_{K^+K^-}$ (e.g. $\ell_{max}=1$ for S-, P-wave description); θ is the angle between the
 4 direction of K^+ and that of the K^+K^- system in the D_s^+ rest frame. The normalizations are

$$\int_{-1}^1 Y_k^0(\cos \theta) Y_j^0(\cos \theta) d \cos \theta = \frac{\delta_{kj}}{2\pi}, \quad (7)$$

5 and it is assumed that the distribution $\frac{dN}{d \cos \theta}$ has been efficiency corrected and background subtracted.

6 Using this orthogonality condition, the coefficients in the expansion are obtained from

$$\langle Y_k^0 \rangle = \int_{-1}^1 Y_k^0(\cos \theta) \frac{dN}{d \cos \theta} d \cos \theta. \quad (8)$$

7 This integral is given, to a good approximation, by $\sum_{n=1}^N Y_k^0(\cos \theta_n)$, where θ_n is the value of θ for the
 8 n -th event.

9 Fig. 12 shows the K^+K^- mass spectrum up to 1.15 GeV/ c^2 weighted by $Y_k^0(\cos \theta) = \sqrt{(2k+1)/(4\pi)} P_k(\cos \theta)$
 10 for $k=0, 1$, and 2, where P_k is the Legendre polynomial function of order k . These distributions are cor-
 11 rected for efficiency and phase space, and background is subtracted by background from generic MC
 12 after BDTG requirement.

13 The number of events N for the mass interval I can be expressed in terms of the partial-wave ampli-
 14 tudes describing the K^+K^- system. Assuming that only S- and P-wave amplitudes are necessary in this
 15 limited region, we can write:

$$\frac{dN}{d \cos \theta} = 2\pi |S Y_0^0(\cos \theta) + P Y_1^0(\cos \theta)|^2. \quad (9)$$

16 By comparing Eq. 6 and 9 [12], we obtain

$$\begin{aligned} \sqrt{4\pi} \langle Y_0^0 \rangle &= |S|^2 + |P|^2, \\ \sqrt{4\pi} \langle Y_2^0 \rangle &= \frac{2}{\sqrt{5}} |P|^2, \end{aligned} \quad (10)$$

17 The above system of equations can be solved in each interval of K^+K^- invariant mass for $|S|$ and $|P|$
 18 and the resulting distributions are shown in Fig. 13.

19 4.4 S-wave Parameterization at the K^+K^- Threshold

20 We empirically parameterize the $S(980)$ with the following function:

$$A_{S(980)} = \frac{1}{m_0^2 - m^2 - im_0 \Gamma_0 \rho_{KK}}, \quad (11)$$

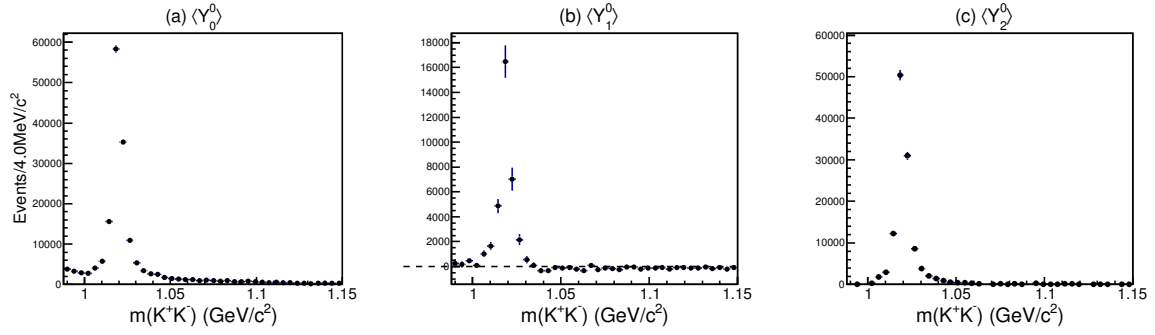


Figure 12: K^+K^- mass spectrum in the threshold region weighted by (a) Y_0^0 , (b) Y_1^0 and (c) Y_2^0 , corrected for efficiency and phase space, and background subtracted.

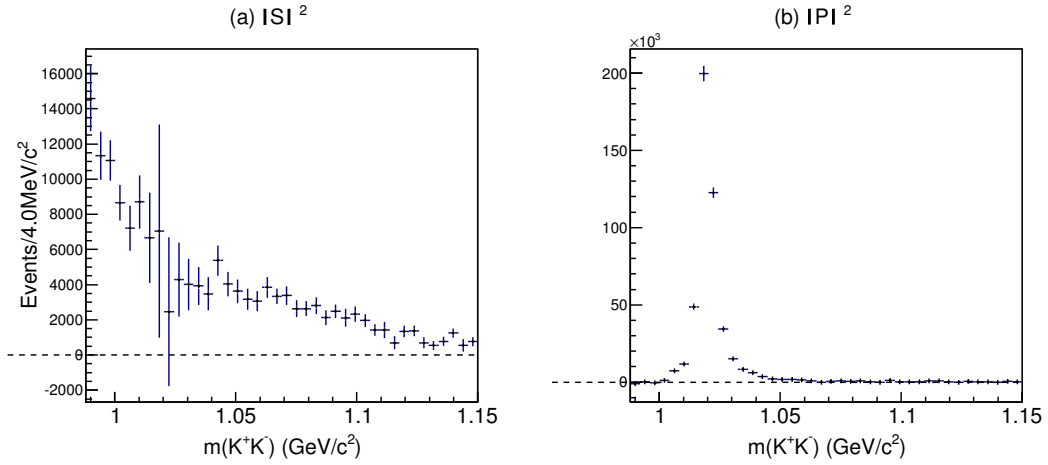


Figure 13: Squared (a) S- and (b) P-wave amplitudes

1 where $\rho_{KK} = 2p/m$, and obtain the following parameter values by fitting the S-wave amplitudes in
 2 Fig. 13 (b) with this Eq. 11.:

$$\begin{aligned} m_0 &= (0.919 \pm 0.006_{stat}) \text{ GeV}/c^2, \\ \Gamma_0 &= (0.272 \pm 0.040_{stat}) \text{ GeV}/c^2. \end{aligned} \quad (12)$$

3 The errors are statistical only. The fit result is shown in Fig. 14.

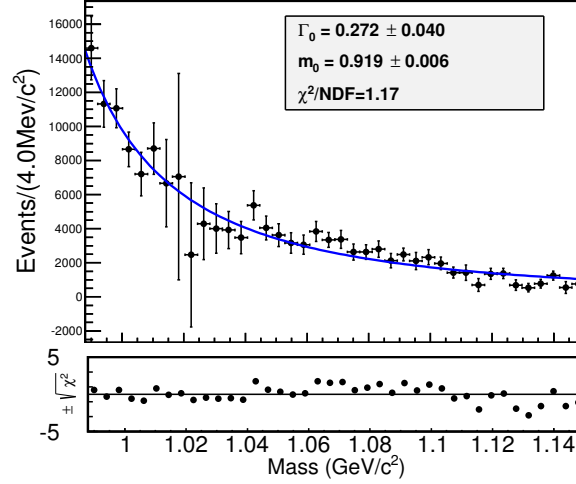


Figure 14: Fit of S-wave amplitudes. The curves result from the fit described in the text.

4 4.5 Systematic Uncertainties

5 Systematic uncertainties take in account:

- 6 • I Data-MC agreement for the BDTG output. We apply the same BDTG as that in Sec. 4.2 to a
 7 control sample, which passed the same event selection without the kinematic fit χ^2_{5c} cut criteria as
 8 that in Sec. 5.1, and compare the efficiency of data and MC. The efficiency of data (MC) is defined
 9 as $e_{data} = \frac{N_{d0}}{N_{d1}}$ ($e_{MC} = \frac{N_{M0}}{N_{M1}}$), where N_{d0} (N_{M0}) and N_{d1} (N_{M1}) are the number of events before
 10 and after applying the BDTG cut criteria. The comparison of efficiencies between data and MC is
 11 listed in Table 5. We fit the shape of S(980) corrected with $\frac{e_{data}}{e_{MC}}$ and take the shift of m_0 and Γ_0 as
 12 the systematic uncertainty. The shift of m_0 and Γ_0 are 0.03 GeV/ c^2 and 0.02 GeV/ c^2 , respectively.
- 13 • II Background subtraction. We change the bin number and fit range and replace the background
 14 shape with a third-order Chebychev polynomial in the fit shown in Fig 9 and take the shift as
 15 a resource of background ratio error. We vary the background ratio ($(3.8 \pm 0.3)\%$) with one
 16 sigma and then take the largest shift of the fit of S(980) as the systematic uncertainty related to the
 17 background ratio. The background shape of generic MC is also replaced with that of “Sideband”

Table 5: The comparison of efficiencies between data and MC.

$m_{K^+K^-}$ (GeV/ c^2)	e_{data}	e_{MC}	e_{data}/e_{MC}
[0.988, 1.014]	0.3134 ± 0.0273	0.3069 ± 0.0062	1.0210 ± 0.0914
[1.014, 1.018]	0.3199 ± 0.0278	0.3641 ± 0.0068	0.8787 ± 0.0781
[1.018, 1.019]	0.3968 ± 0.0357	0.4059 ± 0.0080	0.9775 ± 0.0900
[1.019, 1.021]	0.3631 ± 0.0320	0.3970 ± 0.0083	0.9146 ± 0.0830
[1.021, 1.023]	0.3704 ± 0.0330	0.3834 ± 0.0075	0.9662 ± 0.0881
[1.023, 1.029]	0.3028 ± 0.0261	0.3190 ± 0.0064	0.9491 ± 0.0840
[1.029, 1.061]	0.2932 ± 0.0254	0.2962 ± 0.0059	0.9900 ± 0.0878
[1.061, 1.150]	0.2440 ± 0.0201	0.2502 ± 0.0049	0.9750 ± 0.0829

for data to perform a fit and the shift is taken as the systematic uncertainty related to the background shape. The shift of m_0 and Γ_0 are 0.002 GeV/ c^2 and 0.001 GeV/ c^2 .

- III PID and tracking efficiency difference between data and MC. To estimate the experimental effects related to the difference of PID and tracking efficiency between data and MC, based on the work [13] and the work [14], we weight each event with the efficiency of data divided by that of MC and fit the shape of S(980). The shift of m_0 and Γ_0 are 0.001 GeV/ c^2 and 0.013 GeV/ c^2 .
- IV The $f_0(1370)$ remained in S(980). We assume that the fit fraction (defined in Sec. 5.4) of $D_s^+ \rightarrow f_0(1370)\pi^+$ is 5% and then produced a MC sample with procedure $D_s^+ \rightarrow f_0(1370)\pi^+$ to extract the shape of $f_0(1370)$ at the low end of $m_{K^+K^-}$ mass spectrum. We scale the number of $D_s^+ \rightarrow f_0(1370)\pi^+$ according to the fit fraction of $D_s^+ \rightarrow f_0(1370)\pi^+$ and the shape contributed from $f_0(1370)$ is shown in Fig. 15. At last, the $f_0(1370)$ remained in S(980) is subtracted according to the scaled shape obtained above. The shift of m_0 and Γ_0 are 0.001 GeV/ c^2 and 0.003 GeV/ c^2 .
- V Fit range. We vary the fit range from [0.988, 1.15] GeV/ c^2 to [0.988, 1.145] GeV/ c^2 and the shift of m_0 and Γ_0 are 0.002 GeV/ c^2 and 0.003 GeV/ c^2 .

All of the systematic uncertainties mentioned above are summarized in Table 6. So the result of m_0 and Γ_0 is:

$$\begin{aligned}
 m_0 &= (0.919 \pm 0.006_{stat} \pm 0.030_{sys}) \text{ GeV}/c^2, \\
 \Gamma_\alpha &= (0.272 \pm 0.040_{stat} \pm 0.024_{sys}) \text{ GeV}/c^2,
 \end{aligned} \tag{13}$$

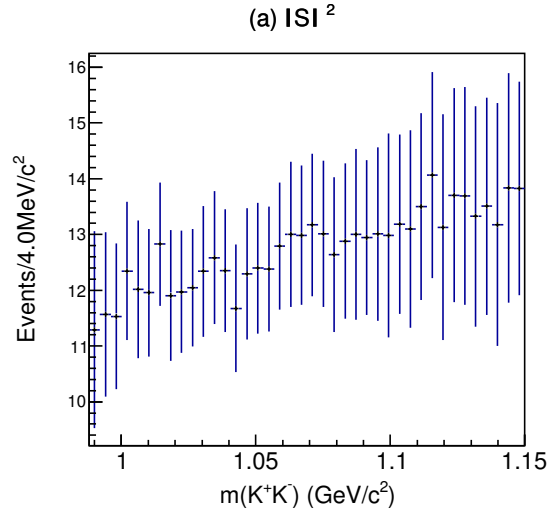


Figure 15: The shape of $f_0(1370)$ at the low end of $m_{K^+K^-}$ mass spectrum extracted from a MC sample with procedure $D_s^+ \rightarrow f_0(1370)\pi^+$.

Table 6: Systematic uncertainties of partial wave analysis in the low K^+K^- mass region.

Source	m_0 (GeV/ c^2)	Γ_0 (GeV/ c^2)
BDTG	0.030	0.020
Background subtraction	0.002	0.001
PID and Tracking	0.001	0.013
$f_0(1370)$	0.001	0.003
Fit range	0.002	0.003
total	0.030	0.024

5 Amplitude Analysis

5.1 Event Selection

After K^\pm , K_S^0 , η , η' , π^\pm and π^0 are identified in Sec. 3, hadronic D_s decays can be reconstructed with the DTag package. Eight tag modes are used:

$$D_s^- \rightarrow K^+ K^- \pi^-, D_s^- \rightarrow K_S^0 K^-, D_s^- \rightarrow K_S^0 K^- \pi^+ \pi^-, D_s^- \rightarrow K^- \pi^+ \pi^-, D_s^- \rightarrow K_S^0 K^+ \pi^- \pi^-, D_s^- \rightarrow \pi^+ \pi^- \pi^-, D_s^- \rightarrow \eta_{\pi^+ \pi^- \eta_{\gamma\gamma}}', D_s^- \rightarrow K^+ K^- \pi^- \pi^0.$$

With the tagged D_s meson, the signal D_s is reconstructed with the remaining good tracks. The momentum of π^\pm (π^0) is required to be larger than 100 MeV/c² to suppress the background of $D^* \rightarrow D\pi$. Only the D_s candidate with invariant mass falls into [1.87, 2.06] GeV/c² are selected.

For every candidate of $D_s D_s^*$ decays, all tracks at signal side and tag side as well as gamma from D_s^* are added to apply kinematic fitting. Five constrains are added in kinematic fitting: four-momentum of $D_s D_s^*$ and mass of D_s^* . Then we select the candidate with minimum χ_{5c}^2 .

The candidates satisfy:

- m_{sig} and m_{tag} falls in the mass regions shown in Table 7,

- $\chi_{5c}^2 < 200$,

are retained for the amplitude analysis, where m_{sig} and m_{tag} refer to mass of D_s at signal side and tag side respectively.

Table 7: The mass windows for each tag mode. The mass windows use the results in Ref. [15]

Tag mode	Mass window (GeV/c ²)
$D_s^- \rightarrow K_S^0 K^-$	[1.948, 1.991]
$D_s^- \rightarrow K^+ K^- \pi^-$	[1.950, 1.986]
$D_s^- \rightarrow K^+ K^- \pi^- \pi^0$	[1.947, 1.982]
$D_s^- \rightarrow K_S^0 K^- \pi^+ \pi^-$	[1.958, 1.980]
$D_s^- \rightarrow K_S^0 K^+ \pi^- \pi^-$	[1.953, 1.983]
$D_s^- \rightarrow \pi^- \pi^- \pi^+$	[1.952, 1.984]
$D_s^- \rightarrow \pi^- \eta_{\pi^+ \pi^- \eta_{\gamma\gamma}}'$	[1.940, 1.996]
$D_s^- \rightarrow K^- \pi^+ \pi^-$	[1.953, 1.983]

5.2 Background Analysis

We use generic MC to estimate the background. The background and signal shape of generic MC is shown in Fig. 16. By scaling the generic MC background sample to the data size based on the luminosities, the background yields in the signal region is 17.2. The fit to the signal D_s invariant mass

- 1 (m_{sig}) spectrum gives the background yield in the signal region is 18.1 ± 5.1 , shown as in Fig. 17. The
 2 background level in generic MC is consistent with the data. In the fit, the signal shape is the MC shape
 3 convoluted with a Gaussian function and the background is the MC shape.

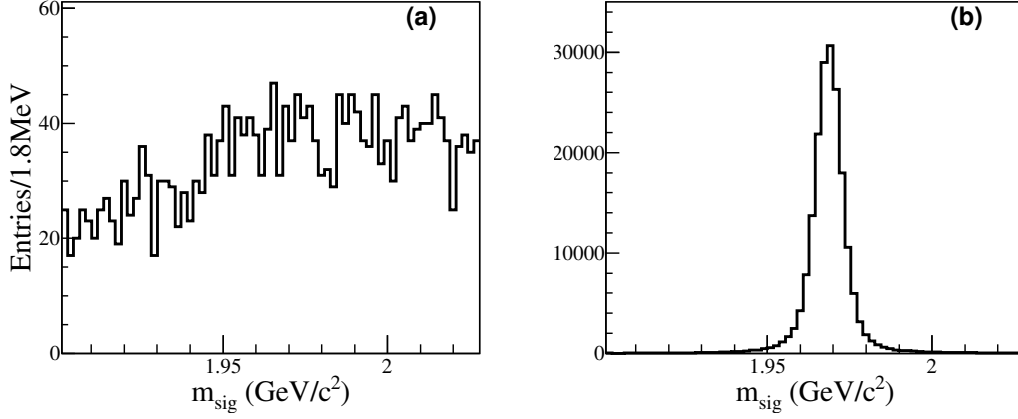


Figure 16: The background and the signal shape of generic MC (round 01-40)

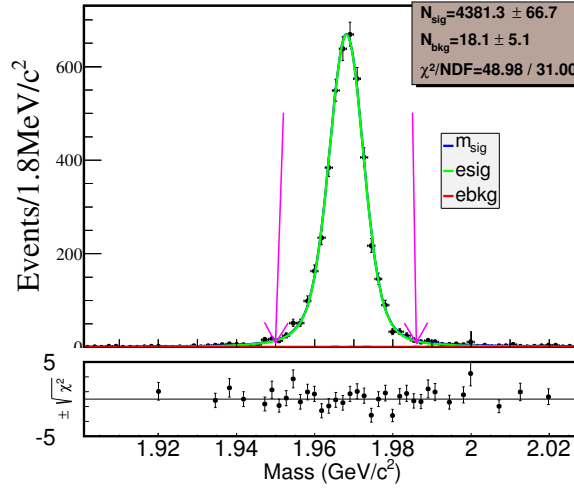


Figure 17: The fit to m_{sig} for data after selections, the area between the purple arrows is the signal area of the sample for the amplitude analysis. The signal shape (green line) is the MC shape convoluted with a Gaussian function and the background (red line) is the MC shape.

4 5.3 Fit Method

5 The method used in the amplitude analysis is the same as the Ref. [16]. In this section, we briefly
 6 review the amplitude analysis method used in this analysis.

7 The relative magnitudes and phases of the partial waves and the mass and width of intermediate
 8 resonances are determined by an unbinned maximum-likelihood fit to the data selected. The formulas

are constructed with covariant tensors [17].

Since there are three final state particles, only one possible resonant state is allowed in any intermediate process. Thus the amplitude of the n^{th} intermediate state (A_n) is,

$$A_n = P_n S_n F_n^r F_n^D, \quad (14)$$

where S_n and $F_n^{r(D)}$ are the spin factor and the Blatt-Weisskopf barriers of the intermediate state (the D_s meson), respectively. P_n is the propagator of the intermediate resonance.

The total amplitude M is then the coherent sum of the amplitudes of intermediate processes, $M = \sum c_n A_n$, where $c_n = \rho_n e^{i\phi_n}$ is the corresponding complex coefficient. The magnitude ρ_n and phase ϕ_n are determined by the amplitude analysis. The signal probability density function (PDF) $f_S(p_j)$ is given by

$$f_S(p_j) = \frac{\epsilon(p_j) |M(p_j)|^2 R_3(p_j)}{\int \epsilon(p_j) |M(p_j)|^2 R_3(p_j) dp_j}, \quad (15)$$

where $\epsilon(p_j)$ is the detection efficiency parameterized in terms of the final four-momenta p_j . The index j refers to the different particles in the final states. $R_3(p_j)$ is the standard element of the three-body phase space. The normalization integral is determined by a MC integration,

$$\int \epsilon(p_j) |M(p_j)|^2 R_3(p_j) dp_j \approx \frac{1}{N_{MC}} \sum_{k_{MC}}^{N_{MC}} \frac{|M(p_j^{k_{MC}})|^2}{|M^{gen}(p_j^{k_{MC}})|^2}, \quad (16)$$

where k_{MC} is the index of the k_{MC}^{th} event of the MC sample and N_{MC} is the number of the selected MC events. $M^{gen}(p_j)$ is the PDF used to generate the MC samples in MC integration. At the beginning, the PHSP MC are used in MC integration. $M^{gen}(p_j)$ is a constant overall the phase space. Then with the result obtained from the fit to data, the signal MC is then generated and used in MC integration. In this analysis, a PHSP MC sample with about 6 million events and a signal MC sample with about 2 million events are used in the normalization integral calculation using PHSP MC and signal MC, respectively. In the numerator of Eq. 15, $\epsilon(p_j)$ is independent of the fitted variables, so it is regarded as a constant term in the fit. Considering the bias caused by particle identification (PID) [13] and tracking [14] efficiency differences between data and MC, we introduce γ_ϵ to correct this bias:

$$\gamma_\epsilon = \prod_i \frac{\epsilon_{i,data}(p_i)}{\epsilon_{i,MC}(p_i)}, \quad (17)$$

where i denotes the three daughter particles.

Since there is only about 0.4% background in the data sample, the contribution from the background is ignored in the likelihood calculation:

$$\ln \mathcal{L} = \sum_k^{N_{data}} \ln f_S(p_j^k), \quad (18)$$

where N_{data} is the number of candidate events in data.

5.3.1 Propagator

For a decay process $a \rightarrow bc$, $s_{a/b/c}$ is denoted to be the invariant mass square of the particle a/b/c, $r_a = p_b - p_c$, and q is denoted as the magnitude of the momentum of daughter particle in the rest system of a

$$q = \sqrt{\frac{(s_a + s_b + s_c)^2}{4s_a} - s_b}. \quad (19)$$

The intermediate resonances $K^*(892)^0$, $\phi(1020)$ and $f_0(1710)$ are parameterized as a relativistic Breit-Wigner (RBW) formula,

$$P = \frac{1}{(m_0^2 - s_a) - im_0\Gamma(m)}, \quad (20)$$

$$\Gamma(m) = \Gamma_0 \left(\frac{q}{q_0}\right)^{2L+1} \left(\frac{m_0}{m}\right) \left(\frac{X_L(q)}{X_L(q_0)}\right)^2,$$

where m_0 and Γ_0 are the mass and the width of the intermediate resonances, and are fixed to the PDG values [11] except the mass and the width of $f_0(1370)$. The mass and width of $f_0(1370)$ are fixed to 1350 MeV/ c^2 and 265 MeV/ c^2 [18], respectively.. The value of q_0 in Eq. 20 is that of q when $s_a = m_0^2$, L denotes the angular momenta and $X_L(q)$ is defined as:

$$\begin{aligned} X_{L=0}(q) &= 1, \\ X_{L=1}(q) &= \sqrt{\frac{2}{z^2+1}}, \\ X_{L=2}(q) &= \sqrt{\frac{13}{9z^4+3z^2+1}}, \end{aligned} \quad (21)$$

where $z = qR$. The R is the effective radius of the intermediate state or D_s meson and set to 3.0 GeV $^{-1}$ for intermediate states and 5.0 GeV $^{-1}$ for D_s meson [16], respectively. This value R is a typical value used by D physics and we will also vary this value as a source of systematical uncertainties.

$K_0^*(1430)^0$ is parameterized with Flatte formula:

$$P_{K_0^*(1430)^0} = \frac{1}{M^2 - s - i(g_1\rho_{K\pi}(s) + g_2\rho_{\eta'K}(s))}, \quad (22)$$

where s is the $K^-\pi^+$ invariant mass squared, $\rho_{K\pi}(s)$ and $\rho_{\eta'K}(s)$ are Lorentz invariant PHSP factor, and $g_{1,2}$ are coupling constants to the corresponding final state. The parameters of $K_0^*(1430)^0$ are fixed to values measured by CLEO [19]. For resonances $f_0(980)$ and $a_0(980)$, as is discussed in Sec. 1.1, we use Eq. 11 to describe the propagator and the values of parameters are fixed to the values in Eq. 12 obtained from the model independent partial wave analysis section (Sec. 4.4).

5.3.2 Blatt-Weisskopf Barriers

The Blatt-Weisskopf barriers are given by

$$\begin{aligned} F_n &= 1, & (S \text{ wave}), \\ F_n &= \sqrt{\frac{z_0^2+1}{z^2+1}}, & (P \text{ wave}), \\ F_n &= \sqrt{\frac{z_0^4+3z_0^2+9}{z^4+3z^2+9}}, & (D \text{ wave}), \end{aligned} \quad (23)$$

where z_0 are qR and q_0R , respectively.

5.3.3 Spin Factors

As the limit of the phase space, we only consider the states with angular momenta no more than 2.

Considering a two-body decay, the spin projection operators are defined as

$$\begin{aligned} P^0(a) &= 1, & (S \text{ wave}), \\ P_{\mu\mu'}^{(1)}(a) &= -g_{\mu\mu'} + \frac{p_{a\mu}p_{a\mu'}}{p_a^2}, & (P \text{ wave}), \\ P_{\mu\nu\mu'\nu'}^{(2)}(a) &= \frac{1}{2}(P_{\mu\mu'}^{(1)}(a)P_{\nu\nu'}^{(1)}(a) + P_{\mu\nu'}^{(1)}(a)P_{\nu\mu}^{(1)}(a)) + \frac{1}{3}P_{\mu\nu}^{(1)}(a)P_{\mu'\nu'}^{(1)}(a), & (D \text{ wave}). \end{aligned} \quad (24)$$

The covariant tensors are given by

$$\begin{aligned} \tilde{t}^{(0)}(a) &= 1, & (S \text{ wave}), \\ \tilde{t}_\mu^{(1)}(a) &= -P_{\mu\mu'}^{(1)}(a)r^{\mu'}, & (P \text{ wave}), \\ \tilde{t}_{\mu\nu}^{(2)}(a) &= P_{\mu\nu\mu'\nu'}^{(2)}(a)r_a^{\mu'}r_a^{\nu'}, & (D \text{ wave}). \end{aligned} \quad (25)$$

The spin factor for $D_s \rightarrow aX$ and then $a \rightarrow bc$ is(a refers to the intermediate resonance),

$$\begin{aligned} S_n &= 1, & (S \text{ wave}), \\ S_n &= \tilde{T}^{(1)\mu}(D_s)\tilde{t}_\mu^{(1)}(a), & (P \text{ wave}), \\ S_n &= \tilde{T}^{(2)\mu}(D_s)\tilde{t}_\mu^{(2)}(a), & (D \text{ wave}), \end{aligned} \quad (26)$$

where the $\tilde{T}^{(1)\mu}(D_s)(\tilde{T}^{(2)\mu}(D_s))$ and $\tilde{t}_\mu^{(1)}(a)(\tilde{t}_\mu^{(2)}(a))$ are the same defined in Ref. [17].

5.4 Fit Fraction

The fit fractions of the individual amplitudes are calculated according to the fit results and are compared to the other measurements. In the calculation, a PHSP MC with neither detector acceptance nor resolution is involved. The fit fraction for an amplitude is defined as

$$FF(n) = \frac{\sum_{k=1}^{N_{gen}} |A_n|^2}{\sum_{k=1}^{N_{gen}} |M(p_j^k)|^2}, \quad (27)$$

where $N_{gen} = 2000000$, is the number of the PHSP MC events at generator level.

To estimate the statistical uncertainties of the fit fractions, we repeat the calculation of fit fractions by randomly varying the fitted parameters according to the error matrix. Then, for each amplitude, we fit the resulting distribution with a Gaussian function, whose width gives the corresponding statistical uncertainty.

5.5 Fit Result

The Dalitz plot of $m^2(K^+K^-)$ versus $m^2(K^-\pi^+)$ is shown in Fig. 18. In the plot, we can see a clear peak of $K^*(892)^0$ and $\phi(1020)$. In the fit, the magnitude and phase of the amplitude $D_s^+ \rightarrow K^*(892)^0 K^+$ is fixed to 1.0 and 0.0, and the magnitudes and phases of the amplitudes are allowed to float.

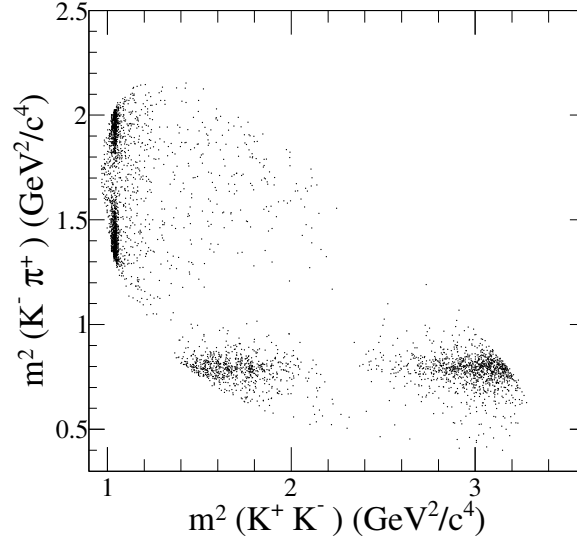


Figure 18: The Dalitz plot of $m^2(K^-\pi^+)$ versus $m^2(K^+K^-)$ after event selection.

With the requiring the statistical significance larger than 5 standard deviations, there are 6 intermediate process, $D_s^+ \rightarrow \bar{K}^*(892)^0 K^+$, $D_s^+ \rightarrow \phi(1020)\pi^+$, $D_s^+ \rightarrow S(980)\pi^+$, $D_s^+ \rightarrow \bar{K}_0^*(1430)^0 K^+$, $D_s^+ \rightarrow f_0(1370)\pi^+$, $D_s^+ \rightarrow f_0(1710)\pi^+$ are retained in the final result. The statistical significance of the three amplitudes in final result are also checked. The statistical significance is calculated by the difference of the likelihood of fits with and without a certain amplitude along with the difference of degree of freedom. The detail $2\Delta(\ln L)$, Δn_{par} , and the statistical significance for each amplitude are listed in Table 8. We also tested some other intermediate resonances. With each tested amplitude added and fit repeated, we get the corresponding likelihood shift ($\Delta(\ln L)$), the number of freedom degree shift (Δn_{par}) and the statistical significance, and the results are listed in Table 9. All tested amplitudes in Table 9 with statistical significances less than 5 are not retained.

The magnitudes, phases, and fit fractions for the six amplitudes are listed in Table 10.

The Dalitz plot projections are shown in Fig. 19. The fit quality is determined by calculating the χ^2 of the fit using an adaptive binning of the $m^2(K^+K^-)$ versus $m^2(K^-\pi^+)$ Dalitz plot that requires each bin contains at least 10 events. The goodness of the nominal fit is $\chi^2 = 290.1/280 = 1.04$.

Table 8: The $2\Delta(\ln L)$, Δn_{par} , and the statistical significance for each amplitude

Amplitude	$2\Delta(\ln L)$	Δn_{par}	Stat. significance
$D_s^+ \rightarrow \bar{K}^*(892)^0 K^+$	3918.6	2	>20
$D_s^+ \rightarrow \phi(1020)\pi^+$	4606.6	2	>20
$D_s^+ \rightarrow S(980)\pi^+$	541.1	2	>20
$D_s^+ \rightarrow \bar{K}_0^*(1430)^0 K^+$	78.8	2	8.6
$D_s^+ \rightarrow f_0(1710)\pi^+$	89.4	2	9.2
$D_s^+ \rightarrow f_0(1370)\pi^+$	45.1	2	6.4

Table 9: The $\Delta(\ln L)$, Δn_{par} , and the statistical significance for tested amplitudes

Amplitude	$2\Delta(\ln L)$	Δn_{par}	Stat. significance
$D_s^+ \rightarrow f_0(1500)\pi^+$	1.6	2	0.8
$D_s^+ \rightarrow \phi(1680)\pi^+$	3.6	2	1.4
$D_s^+ \rightarrow f_2(1270)\pi^+$	9.0	2	2.5
$D_s^+ \rightarrow f_2(1525)\pi^+$	0.4	2	0.2
$D_s^+ \rightarrow \bar{K}_1^*(1410)^0 K^+$	9.6	2	2.6
$D_s^+ \rightarrow \bar{K}_1^*(1680)^0 K^+$	0.2	2	0.1
$D_s^+ \rightarrow \bar{K}_2^*(1430)^0 K^+$	5.6	2	1.9
non-resonance	12.8	2	3.1

Table 10: The magnitudes, phases and fit fractions for the six amplitudes

Amplitude	Magnitude	Phase	Fit fractions(%)
$D_s^+ \rightarrow \bar{K}^*(892)^0 K^+$	1.0(fixed)	0.0(fixed)	48.3±0.9
$D_s^+ \rightarrow \phi(1020)\pi^+$	1.09±0.02	6.22±0.07	40.5±0.7
$D_s^+ \rightarrow S(980)\pi^+$	2.88±0.14	4.77±0.07	19.3±1.7
$D_s^+ \rightarrow \bar{K}_0^*(1430)^0 K^+$	1.26±0.14	2.91±0.20	3.0±0.6
$D_s^+ \rightarrow f_0(1710)\pi^+$	0.79±0.08	1.02±0.12	1.9±0.4
$D_s^+ \rightarrow f_0(1370)\pi^+$	0.58±0.08	0.59±0.17	1.2±0.4

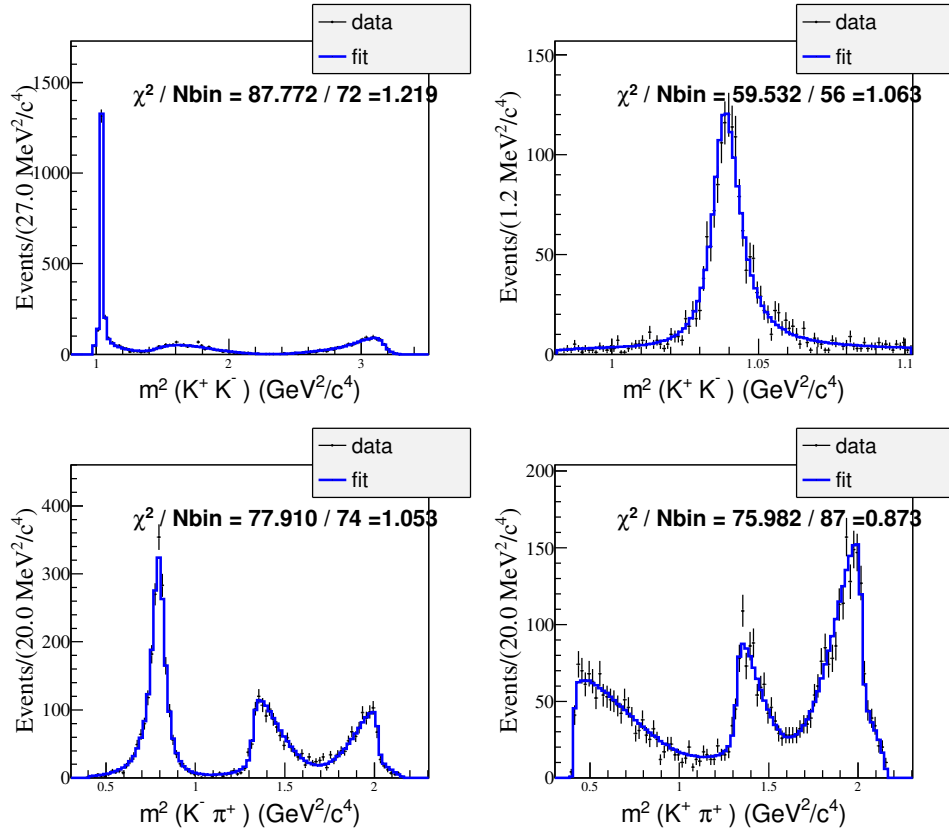


Figure 19: $D_s^+ \rightarrow K^+ K^- \pi^+$: Dalitz plot projections from the nominal fit. The data are represented by points with error bars, the fit results by the histograms.

Table 11: The results of pull distribution checks for the magnitudes, phases and fit fractions for different amplitudes.

Amplitude	Phase		Magnitude		Fit fraction	
	mean	width	mean	width	mean	width
$D_s^+ \rightarrow \bar{K}^*(892)^0 K^+$					-0.13 ± 0.04	0.98 ± 0.03
$D_s^+ \rightarrow \phi(1020) \pi^+$	-0.04 ± 0.05	1.00 ± 0.03	0.07 ± 0.04	0.95 ± 0.03	0.01 ± 0.04	0.95 ± 0.03
$D_s^+ \rightarrow S(980) \pi^+$	-0.07 ± 0.05	1.01 ± 0.03	0.07 ± 0.05	1.10 ± 0.04	0.02 ± 0.05	1.14 ± 0.04
$D_s^+ \rightarrow \bar{K}_0^*(1430)^0 K^+$	0.00 ± 0.05	1.11 ± 0.04	0.14 ± 0.04	0.95 ± 0.03	0.10 ± 0.04	0.99 ± 0.03
$D_s^+ \rightarrow f_0(1710) \pi^+$	0.00 ± 0.04	0.98 ± 0.03	0.08 ± 0.04	0.97 ± 0.03	0.01 ± 0.04	0.99 ± 0.03
$D_s^+ \rightarrow f_0(1370) \pi^+$	-0.11 ± 0.05	1.10 ± 0.04	0.21 ± 0.04	0.99 ± 0.03	0.15 ± 0.04	0.98 ± 0.03

5.6 Systematic Uncertainties

Systematic uncertainties take in account:

- I Variation of masses and widths of resonances within one σ error.
 - For $S(980)$, m_0 and Γ_0 are shifted within errors from Eq. 13 in Sec. 4.5.
 - For $f_0(1370)$, the mass and width are shifted within errors from Ref. [18].
 - For other states, uncertainties are taken from PDG [11].
- II Variation of the effective radius of Blatt-Weisskopf Barrier within the range $[1.0, 5.0] \text{ GeV}^{-1}$ for intermediate resonances and $[3.0, 7.0] \text{ GeV}^{-1}$ for D_s mesons.
- III Fit bias. The possible bias is given by the result from pull distribution check. With the results obtained from the fit, the signal MC samples are generated with the same size of the data. In this analysis, 300 MC samples with the size equaling to data are used to perform the pull distribution check. The results are listed in Table 11. The corresponding plots are shown in Fig. 20, Fig. 21 and Fig. 22. The quadrature sum of the difference of the mean and the nominal value and the error of mean is considered as the uncertainty associated with fit bias.
- IV Experimental effects. The experimental effects are related to the acceptance difference between MC and data caused by PID and tracking efficiencies, that is γ_ϵ in Eq. 17. To estimate the uncertainties caused by γ_ϵ , the amplitude fit is performed varying PID and tracking efficiencies according to their uncertainties according to the work [13] and the work [14].
- V Model assumptions. We replace Eq. 22 with LASS model [20]. And then take the shift of parameters as the uncertainties.

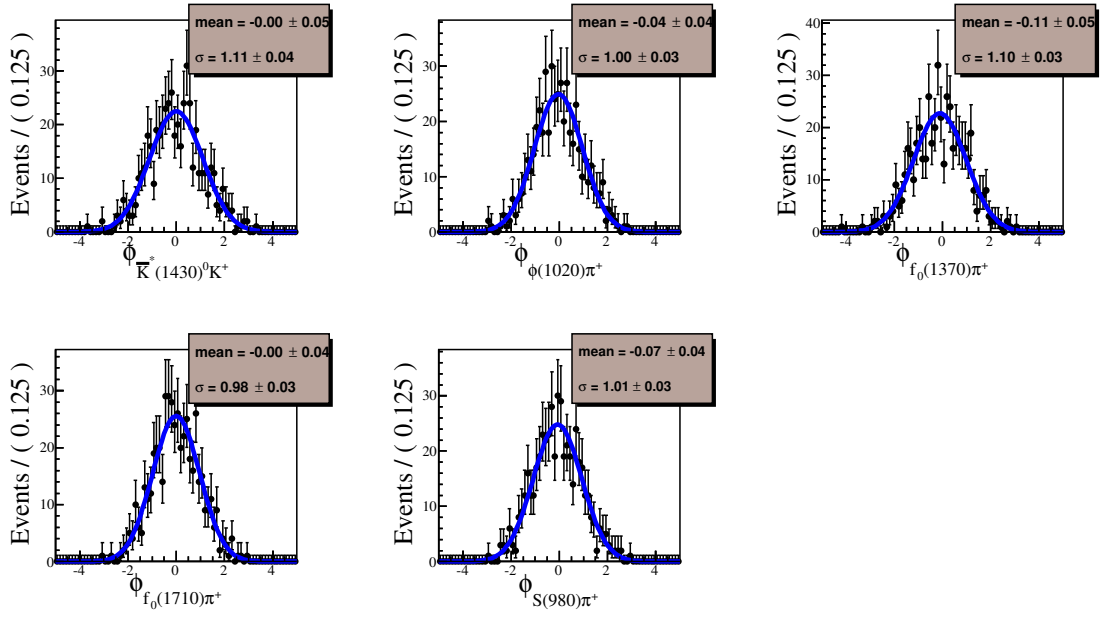


Figure 20: The pull distribution check results for phases of the amplitudes in the nominal fit model.

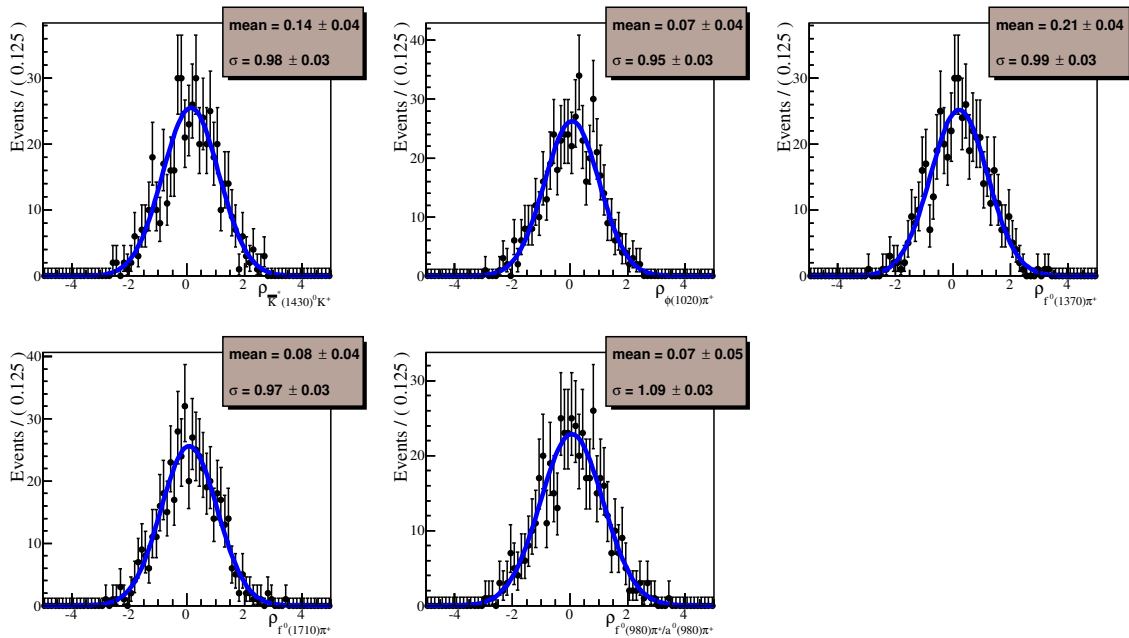


Figure 21: The pull distribution check results for magnitudes of the amplitudes in the nominal fit model.

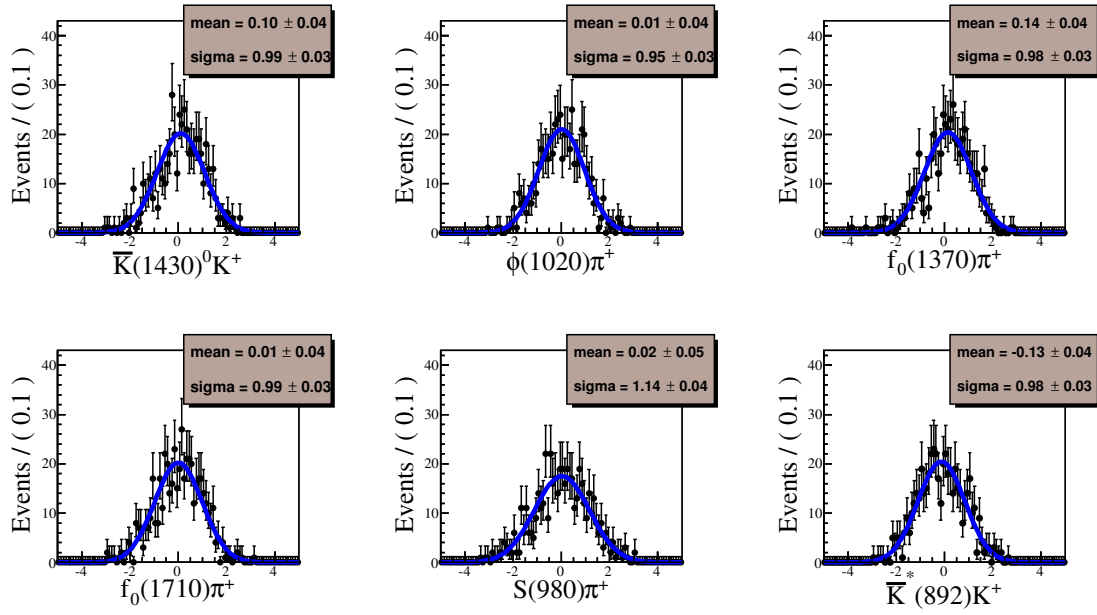


Figure 22: The pull distribution check results for fit fractions of the amplitudes in the nominal fit model.

21 The detail results of the systematic uncertainties are summarized in Table 12. The final results of the
 1 amplitude analysis are then listed in Table 13.

Table 12: Systematic uncertainties on the ϕ and FFs for different amplitudes in units of the corresponding statistical uncertainties.

Amplitude		Source					Total
		I	II	III	IV	V	
$D_s^+ \rightarrow \bar{K}^*(892)^0 K^+$	FF	0.32	0.29	0.13	0.41	0.12	0.62
	ϕ	0.49	0.10	0.06	0.07	0.05	0.51
$D_s^+ \rightarrow \phi(1020)\pi^+$	ρ	0.49	0.14	0.18	0.41	0.15	0.69
	FF	0.44	1.13	0.05	0.40	0.06	1.28
	ϕ	0.98	0.25	0.06	0.11	0.04	1.02
$D_s^+ \rightarrow S(980)\pi^+$	ρ	1.11	0.17	0.10	0.11	0.20	1.15
	FF	1.16	0.15	0.06	0.09	0.05	1.18
	ϕ	1.02	0.48	0.09	0.21	0.07	1.15
$D_s^+ \rightarrow \bar{K}_0^*(1430)^0 K^+$	ρ	1.00	0.36	0.13	0.20	0.14	1.10
	FF	0.76	0.35	0.11	0.22	0.11	0.88
	ϕ	0.31	0.25	0.09	0.14	0.13	0.45
$D_s^+ \rightarrow f_0(1710)\pi^+$	ρ	1.17	1.23	0.07	0.11	0.09	1.70
	FF	0.71	1.21	0.05	0.16	0.04	1.42
	ϕ	2.66	0.27	0.11	0.09	0.21	2.68
$D_s^+ \rightarrow f_0(1370)\pi^+$	ρ	1.01	0.32	0.06	0.09	0.04	1.06
	FF	0.42	0.30	0.15	0.06	0.13	0.56
	ϕ						

Table 13: The final results of the magnitudes, phases and fit fractions for the six amplitudes. The first and second uncertainties are the statistical and systematic uncertainties, respectively.

Amplitude	Magnitude	Phase	Fit fractions (%)
$D_s^+ \rightarrow \bar{K}^*(892)^0 K^+$	1.0 (fixed)	0.0 (fixed)	$48.3 \pm 0.9 \pm 0.6$
$D_s^+ \rightarrow \phi(1020)\pi^+$	$1.09 \pm 0.02 \pm 0.01$	$6.22 \pm 0.07 \pm 0.04$	$40.5 \pm 0.7 \pm 0.9$
$D_s^+ \rightarrow S(980)\pi^+$	$2.88 \pm 0.14 \pm 0.16$	$4.77 \pm 0.07 \pm 0.07$	$19.3 \pm 1.7 \pm 2.0$
$D_s^+ \rightarrow \bar{K}_0^*(1430)^0 K^+$	$1.26 \pm 0.14 \pm 0.15$	$2.91 \pm 0.20 \pm 0.23$	$3.0 \pm 0.6 \pm 0.5$
$D_s^+ \rightarrow f_0(1710)\pi^+$	$0.79 \pm 0.08 \pm 0.14$	$1.02 \pm 0.12 \pm 0.05$	$1.9 \pm 0.4 \pm 0.6$
$D_s^+ \rightarrow f_0(1370)\pi^+$	$0.58 \pm 0.08 \pm 0.08$	$0.59 \pm 0.17 \pm 0.46$	$1.2 \pm 0.4 \pm 0.2$

6 Branching Fraction Measurements

6.1 Event Selection

After the selection described in Sec. 3, we further use the double tag technique for the BF (branching fraction) measurement. We use the same 8 tag modes as in Sec. 5.1. In the selection of tag D_s , for multiple candidates, the best candidate is chosen with M_{rec} closest to mass of D_s^* in [11]. To further remove the background associated with the larger number of soft π^\pm (π^0) from D_s^* decays, candidates are voted if the momentum of π^\pm (π^0) is less than 0.1 GeV.

The single tag (ST) yields are extracted from the fits to the D_s invariant mass distributions, as shown in Fig. 23. In the fit, the mass windows of the tag modes are set to be the same as the Ref. [15]. The signal shape is modeled as MC shape convoluted with a Gaussian function, while background is parameterized as the second-order Chebychev polynomial. The corresponding ST efficiencies are estimated from generic MC. The ST yields (Y_{ST}) and ST efficiencies (ϵ_{ST}) are listed in Table 14.

Table 14: The ST yields (Y_{ST}) and ST efficiencies (ϵ_{ST}). The mass windows use the results in Ref. [15]. The BFs of the sub-particle (K_S^0 , π^0 , η and η') decays are not included.

Tag mode	Mass window (GeV/ c^2)	Y_{ST}	$\epsilon_{ST}(\%)$
$D_s^- \rightarrow K_S^0 K^-$	[1.948, 1.991]	32399 ± 274	49.48 ± 0.07
$D_s^- \rightarrow K^+ K^- \pi^-$	-	141189 ± 643	42.17 ± 0.03
$D_s^- \rightarrow K^+ K^- \pi^- \pi_{\gamma\gamma}^0$	[1.947, 1.982]	37899 ± 1739	10.61 ± 0.03
$D_s^- \rightarrow K_S^0 K^- \pi^+ \pi^-$	[1.958, 1.980]	7999 ± 236	19.30 ± 0.12
$D_s^- \rightarrow K_S^0 K^+ \pi^- \pi^-$	[1.953, 1.983]	15723 ± 290	22.72 ± 0.06
$D_s^- \rightarrow \pi^- \pi^- \pi^+$	[1.952, 1.984]	38157 ± 873	56.94 ± 0.17
$D_s^- \rightarrow \pi^- \eta'_{\pi^+ \pi^- \eta_{\gamma\gamma}}$	[1.940, 1.996]	8009 ± 142	20.43 ± 0.06
$D_s^- \rightarrow K^- \pi^+ \pi^-$	[1.953, 1.983]	17112 ± 561	47.18 ± 0.22

After a tag is identified, we search for the $D_s^+ \rightarrow K^+ K^- \pi^+$ signal process. For each tag mode, we may have duplicate signal candidates and the candidates with the minimum average mass (aM) of tag D_s and signal D_s are retained.

With the updated MC sample (DIY MC) based on the amplitude analysis results, the double efficiencies are determined and listed in Table 15.

6.2 Analytic Strategy

The data sample for this analysis is collected at $E_{cm} = 4.178$ GeV, about 100 MeV higher than $D_s^* D_s$ threshold. Around this energy region, based on the cross section measurement by CLEO [9], we know that most D_s production in $e^+ e^-$ collision comes from $D_s^{*\pm} D_s^\mp$ events with a cross section approximate

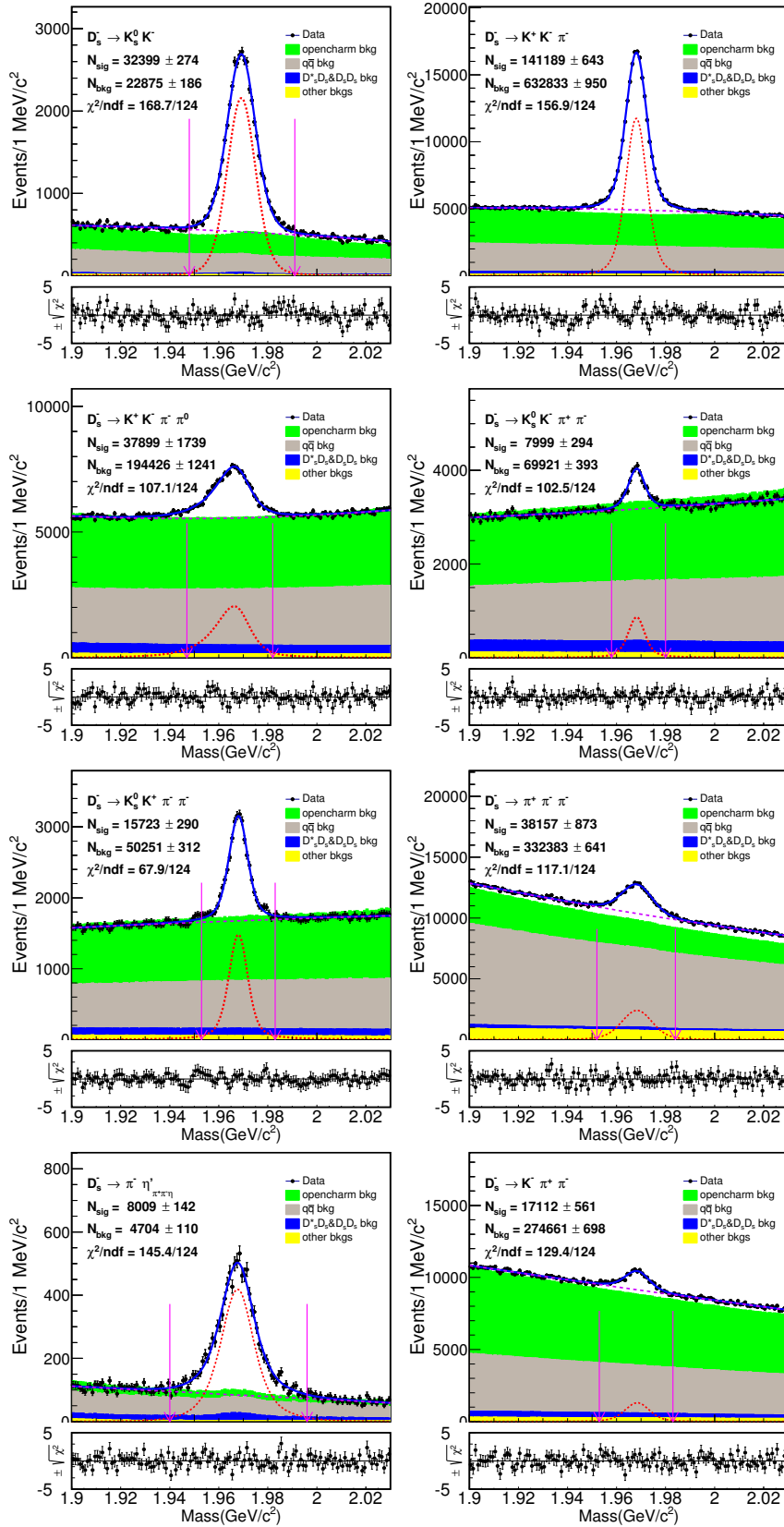


Figure 23: D_s Mass fits from data. The points with error bars are data, and the blue line is the fit. Red short-dashed lines are signal, violet long-dashed lines are background. The red arrows denote the signal region.

Table 15: The DT efficiencies (ϵ_{DT}). The BF's of the sub-particle (K_S^0 , π^0 , η and η') decays are not included.

Tag mode	$\epsilon_{DT}(\%)$
$D_s^- \rightarrow K_S^0 K^-$	19.77 ± 0.14
$D_s^- \rightarrow K^+ K^- \pi^-$	17.41 ± 0.06
$D_s^- \rightarrow K^+ K^- \pi^- \pi^0$	4.69 ± 0.03
$D_s^- \rightarrow K_S^0 K^- \pi^+ \pi^-$	8.04 ± 0.11
$D_s^- \rightarrow K_S^0 K^+ \pi^- \pi^-$	9.35 ± 0.09
$D_s^- \rightarrow \pi^- \pi^- \pi^+ \pi^+$	23.72 ± 0.15
$D_s^- \rightarrow \pi^- \eta'_{\pi^+ \pi^- \eta_{\gamma\gamma}}$	8.70 ± 0.11
$D_s^- \rightarrow K^- \pi^+ \pi^-$	19.68 ± 0.13

1 nb, while the cross section for $D_s^+ D_s^-$ is about a factor of 20 smaller. The D_s^* decays to either γD_s or $\pi^0 D_s$ with branching fractions of $(93.5 \pm 0.7)\%$ and $(5.8 \pm 0.7)\%$ [11], respectively. The other charm productions have a total cross section of 8 nb. The underlying light quark “continuum” background is about 14 nb. The relatively large cross sections, relatively large branching fractions, and sufficient luminosities allow us to employ double tag (DT) technique to study this study.

As $D_s^- \rightarrow K^+ K^- \pi^-$ is not only our signal mode but also one of our tag modes, we divide the events into two categories:

- Cat. A: Tag D_s decays to tag modes except $D_s^- \rightarrow K^+ K^- \pi^-$. The generic MC sample with the signal removed shows no peaking background around the fit range of $1.90 < M_{sig} < 2.03 \text{ GeV}/c^2$. Thus, the double tag yield is determined by the fit to M_{sig} , shown in Fig. 24(a). The background is described with second-order Chebychev polynomial. The double tag yield is 3497 ± 64 .
- Cat. B: Tag D_s decays $K^+ K^- \pi^+$. As both of the two D_s mesons decay to our signal modes, we fit aM (the average mass of D_s at signal side and tag side), which is shown in Fig. 24(b). Here, the background is described by a second-order Chebychev polynomial. The double tag yield is 1651 ± 42 .

To measure the branching fraction of this decay, we start from the following equations with one tag mode:

$$N_{tag}^{obs} = 2N_{D_s^+ D_s^-} \mathcal{B}_{tag} \epsilon_{tag}, \quad (28)$$

$$\begin{aligned} N_{sig}^{obsA} &= 2N_{D_s^+ D_s^-} \mathcal{B}_{tag} \mathcal{B}_{sig} \epsilon_{tag, sig}, & \text{for Cat. A} \\ N_{sig}^{obsB} &= N_{D_s^+ D_s^-} \mathcal{B}_{tag} \mathcal{B}_{sig} \epsilon_{tag, sig}, & \text{for Cat. B} \end{aligned} \quad (29)$$

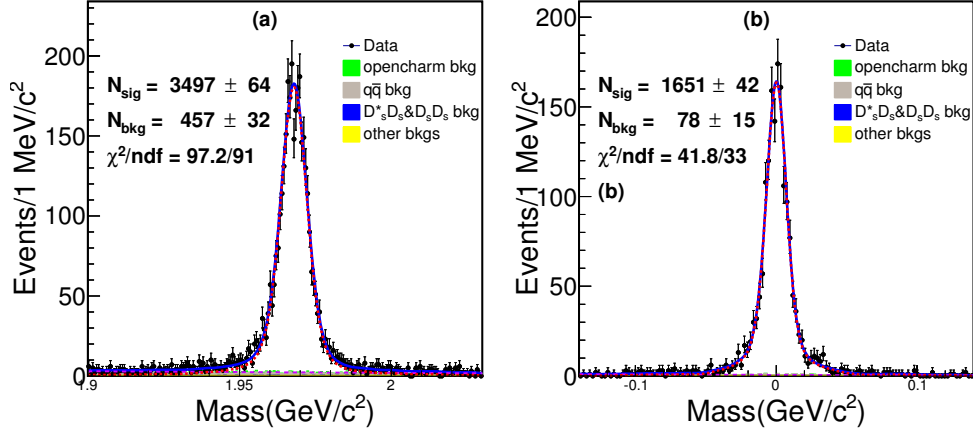


Figure 24: Fit of (a)Cat. A and (b)Cat. B. We fit M_{sig} and aM for Cat. A and Cat. B, respectively. The signal shapes are the corresponding simulated shapes convoluted with a Gaussian function and the background shapes are described with second-order Chebychev polynomial.

where $N_{D_s^+ D_s^-}$ is the total number of $D_s^{*\pm} D_s^\mp$ produced from $e^+ e^-$ collision; N_{tag}^{obs} is the number of observed tag modes; N_{sig}^{obsA} and N_{sig}^{obsB} are the number of observed signals for Cat. A and Cat. B, respectively; \mathcal{B}_{tag} and \mathcal{B}_{sig} are the branching fractions of a specific tag mode and the signal mode, respectively; ϵ_{tag} is the efficiency to reconstruct the tag mode; $\epsilon_{tag,sig}$ is the efficiency to reconstruct both the tag and signal decay modes.

Using the above equations, it's easy to obtain:

$$\mathcal{B}_{sig} = \frac{N_{sig}^{obsA} + 2N_{sig}^{obsB}}{\sum_{\alpha} N_{tag}^{\alpha} \epsilon_{tag,sig}^{\alpha} / \epsilon_{tag}^{\alpha}}, \quad (30)$$

where the yields N_{tag}^{obsA} , N_{tag}^{obsB} and N_{tag}^{α} are obtained from data, while ϵ_{tag} and $\epsilon_{tag,sig}$ can be obtained from the appropriate MC samples, where α represents the tag modes.

6.3 Results of Branching Fraction

We determine the branching fraction $\mathcal{B}(D_s^+ \rightarrow K^+ K^- \pi^+) = (5.47 \pm 0.07)\%$ (statistical uncertainty only) according to Eq. 30.

6.4 Systematic Uncertainties

The following sources are taken in account to calculate systematic uncertainties.

- Uncertainty in the number of ST D_s^- candidates. We perform alternative fits with different background shapes, signal shapes, fit ranges and bin sizes to obtain the uncertainties related to the corresponding factors. We change the background shape from the second-order Chebychev polynomial to a third-order Chebychev polynomial and the relative change of branching fraction is

0.18%. The systematic in signal shape is determined to be 0.16% by performing an alternative fit without convolving the Gaussian resolution function. For fit range, we vary the fit range from $[1.90, 2.03] \text{ GeV}/c^2$ to $[1.90, 2.02] \text{ GeV}/c^2$ and the relative difference of branching fraction is 0.24%. According to Table 14, the total ST yields of the eight tag modes is 298487 ± 2186 . Then the uncertainty due to background fluctuation is $2186/298487 = 0.73\%$. The quadrature sum of these terms, that is the uncertainty in the number of ST D_s^- candidates, is 0.84%.

- Signal shape. The systematic uncertainty due to the signal shape is studied with the fit without the Gaussian function convoluted, the double tag yield shift is taken as the related effect.
- Background shape and fit range. For background shape and the fit range in the fit, the first-order Chebychev polynomial is used to replace the nominal ones and the fit range of $[1.90, 2.03] \text{ GeV}/c^2$ for Cat. A and $[-0.14, 0.13] \text{ GeV}/c^2$ are changed to $[1.90, 2.02] \text{ GeV}/c^2$ and $[-0.13, 0.13] \text{ GeV}/c^2$ respectively. The largest branching fraction shift is taken as the related effect.
- Fit bias. The possible bias is estimated by the input/output check using the round 30-40 of generic MC, which is shown in Table 16. The estimated mean (μ_B) and its uncertainty (σ_μ) is calculated with the following formulas:

$$\mu_B = \frac{\sum_i \frac{\mu_i}{\sigma_i^2}}{\sum_i \frac{1}{\sigma_i^2}}, \quad \sigma_\mu^2 = \sum_i \frac{1}{\sigma_i^2}, \quad (31)$$

where μ_i and σ_i are the measured branching fraction value and its statistical uncertainty for the sample i. The combined result of the round 30-40 is $\mu_B = (5.462 \pm 0.021)\%$. The relative change compared to the input value is 0.1%, which is very small and negligible.

Table 16: Input/output check using the round 30-40 of generic MC.

Round	$\mathcal{B}(D_s^+ \rightarrow K^+ K^- \pi^+)(\%)$
31	5.562 ± 0.066
32	5.497 ± 0.066
33	5.407 ± 0.066
34	5.636 ± 0.068
35	5.490 ± 0.066
36	5.397 ± 0.066
37	5.369 ± 0.066
38	5.490 ± 0.067
39	5.353 ± 0.065
40	5.435 ± 0.066
Combined result	5.462 ± 0.021

- K^\pm and π^\pm Tracking/PID efficiency. Based on the works [13] and [14] by Xingyu Shan and Sanqiang Qu, etc. we find that it's enough to assign 1.1% , 0.4%, 1.1% and 0.2% as the systematic uncertainty for K^\pm PID, π^\pm PID, K^\pm tracking, π^\pm tracking efficiencies, respectively.
- MC statistics. The uncertainty of MC statistics is obtained by $\sqrt{\sum_i f_i \frac{\delta_{\epsilon_i}}{\epsilon_i}}$, where f_i is the tag yield fraction and ϵ_i is the signal efficiency of tag mode i .
- Dalitz model. The uncertainty from the Dalitz model is estimated as the change of efficiency when the Dalitz model parameters are varied by their uncertainties.

All of the systematic uncertainties mentioned above are summarized in Table 17.

Table 17: Systematic uncertainties of branching fraction.

Source	Sys. Uncertainty
Number of D_s^-	0.8
Signal shape	0.5
Background shape and fit range	0.9
K^\pm and π^\pm PID efficiency	1.5
K^\pm and π^\pm Tracking efficiency	1.3
MC statistics	0.2
Dalitz model	0.5
total	2.4

The branching fraction with systematic uncertainties is $\mathcal{B}(D_s^+ \rightarrow K^+ K^- \pi^+) = (5.47 \pm 0.07_{stat.} \pm 0.13_{sys.})\%$. Using the FFs listed in Table 12, the BF's for the intermediate processes can be calculated with $\mathcal{B}_i = FF_i \times \mathcal{B}(D_s^+ \rightarrow K^+ K^- \pi^+)$, which are listed in Table 18.

Table 18: The branching fractions for the intermediate processes.

Intermediate process	Branching fractions (%)
$D_s^+ \rightarrow \bar{K}^*(892)^0 K^+$	$2.62 \pm 0.04_{stat.} \pm 0.09_{sys.}$
$D_s^+ \rightarrow \phi(1020) \pi^+$	$2.26 \pm 0.05_{stat.} \pm 0.08_{sys.}$
$D_s^+ \rightarrow S(980) \pi^+$	$0.90 \pm 0.04_{stat.} \pm 0.11_{sys.}$
$D_s^+ \rightarrow \bar{K}_0^*(1430)^0 K^+$	$0.13 \pm 0.02_{stat.} \pm 0.05_{sys.}$
$D_s^+ \rightarrow f_0(1710) \pi^+$	$0.06 \pm 0.01_{stat.} \pm 0.01_{sys.}$
$D_s^+ \rightarrow f_0(1370) \pi^+$	$0.06 \pm 0.01_{stat.} \pm 0.01_{sys.}$

7 Summary

This analysis presents the amplitude analysis of the decay $D_s^+ \rightarrow K^+ K^- \pi^+$. Table 19 is a comparison of amplitude analysis between BABAR, CLEO-c and this analysis. Our results are roughly consistent with those of BABAR and CLEO-c. For the fit fraction of $D_s^+ \rightarrow f_0(980)\pi^+ / a_0(980)\pi^+$, we tend to agree with the result of BABAR.

Table 19: Comparison of fit fraction between BABAR, CLEO-c and this amplitude analysis.

Amplitude	BABAR	CLEO-c	This Analysis
$D_s^+ \rightarrow \bar{K}^*(892)^0 K^+$	$47.9 \pm 0.5 \pm 0.5$	$47.4 \pm 1.5 \pm 0.4$	$48.3 \pm 0.9 \pm 0.6$
$D_s^+ \rightarrow \phi(1020)\pi^+$	$41.4 \pm 0.8 \pm 0.5$	$42.2 \pm 1.6 \pm 0.3$	$40.5 \pm 0.7 \pm 0.9$
$D_s^+ \rightarrow S(980)\pi^+$	$16.4 \pm 0.7 \pm 2.0$	$28.2 \pm 1.9 \pm 1.8$	$19.3 \pm 1.7 \pm 2.0$
$D_s^+ \rightarrow \bar{K}_0^*(1430)^0 K^+$	$2.4 \pm 0.3 \pm 1.0$	$3.9 \pm 0.5 \pm 0.5$	$3.0 \pm 0.6 \pm 0.5$
$D_s^+ \rightarrow f_0(1710)\pi^+$	$1.1 \pm 0.1 \pm 0.1$	$3.4 \pm 0.5 \pm 0.3$	$1.9 \pm 0.4 \pm 0.6$
$D_s^+ \rightarrow f_0(1370)\pi^+$	$1.1 \pm 0.1 \pm 0.2$	$4.3 \pm 0.6 \pm 0.5$	$1.2 \pm 0.4 \pm 0.2$
$\sum FF(\%)$	$110.2 \pm 0.6 \pm 2.0$	$129.5 \pm 4.4 \pm 2.0$	$114.2 \pm 1.7 \pm 2.3$
χ^2/NDF	$\frac{2843}{2305-14} = 1.2$	$\frac{178}{117} = 1.5$	$\frac{290}{291-10-1} = 1.04$
Events	96307 ± 369 (purity 95%)	14400(purity 85%)	4381(purity 99.7%)

In this analysis, as $a_0(980)$ and $f_0(980)$ overlap and parameters of $f_0(980)$ is not well measured, we have extracted the S -wave lineshape in the low end of $K^+ K^-$ mass spectrum with the model independent method.

We also measure the branching fraction $\mathcal{B}(D_s^+ \rightarrow K^+ K^- \pi^+) = (5.47 \pm 0.07_{stat.} \pm 0.13_{sys.})\%$. As is shown in Table 20, the branching fraction of this analysis has the best precision.

Table 20: Comparisons of branching fraction between BABAR, CLEO-c and this analysis.

$\mathcal{B}(D_s^+ \rightarrow K^+ K^- \pi^+)(\%)$	Collaboration
$5.55 \pm 0.14_{stat.} \pm 0.13_{sys.}$	CLEO-c [22]
$5.06 \pm 0.15_{stat.} \pm 0.21_{sys.}$	BELLE [23]
$5.78 \pm 0.20_{stat.} \pm 0.30_{sys.}$	BABAR [24]
$5.47 \pm 0.07_{stat.} \pm 0.13_{sys.}$	BESIII(this analysis)

We also obtained the branching fractions for the intermediate processes, listed in Table 21. According to the Eq. 2 in Sec. 1.1, we can obtain $\mathcal{B}(D_s^+ \rightarrow a_0(980)\pi^+, a_0(980) \rightarrow K^+ K^-)$ is about 0.14%, which is much less than $\mathcal{B}(D_s^+ \rightarrow S(980)\pi^+)$ listed in Table 21. We can see that $\mathcal{B}(D_s^+ \rightarrow S(980)\pi^+)$ measured in this analysis is not inconsistent with the one obtained in the Dalitz plot analysis of $D_s^+ \rightarrow$

Table 21: The branching fractions measured in this analysis.

Process	Branching fractions (%)
$D_s^+ \rightarrow \bar{K}^*(892)^0 K^+, \bar{K}^*(892)^0 \rightarrow K^- \pi^+$	$2.62 \pm 0.04_{stat.} \pm 0.07_{sys.}$
$D_s^+ \rightarrow \phi(1020) \pi^+, \phi(1020) \rightarrow K^+ K^-$	$2.26 \pm 0.05_{stat.} \pm 0.06_{sys.}$
$D_s^+ \rightarrow S(980) \pi^+, S(980) \rightarrow K^+ K^-$	$0.90 \pm 0.04_{stat.} \pm 0.11_{sys.}$
$D_s^+ \rightarrow \bar{K}_0^*(1430)^0 K^+, \bar{K}_0^*(1430)^0 \rightarrow K^- \pi^+$	$0.13 \pm 0.02_{stat.} \pm 0.05_{sys.}$
$D_s^+ \rightarrow f_0(1710) \pi^+, f_0(1710) \rightarrow K^+ K^-$	$0.06 \pm 0.01_{stat.} \pm 0.01_{sys.}$
$D_s^+ \rightarrow f_0(1370) \pi^+, f_0(1370) \rightarrow K^+ K^-$	$0.06 \pm 0.01_{stat.} \pm 0.01_{sys.}$
$D_s^+ \rightarrow K^+ K^- \pi^+$ total branching fraction	$5.47 \pm 0.07_{stat.} \pm 0.13_{sys.}$

2 $\pi^+ \pi^0 \eta$ [1]. With $\mathcal{B}(\bar{K}^*(892)^0 \rightarrow K^- \pi^+)$ and $\mathcal{B}(\phi(1020) \rightarrow K^+ K^-)$ from PDG [11], we can obtain
3 $\mathcal{B}(D_s^+ \rightarrow \bar{K}^*(892)^0 K^+) = (3.94 \pm 0.12)\%$ and $\mathcal{B}(D_s^+ \rightarrow \phi(1020) \pi^+) = (4.60 \pm 0.17)\%$. The com-
4 parison of $\mathcal{B}(D_s^+ \rightarrow \bar{K}^*(892)^0 K^+)$ and $\mathcal{B}(D_s^+ \rightarrow \phi(1020) \pi^+)$ between this analysis and some theory
5 predictions [5] is listed in Table 22. Our results are consistent with theory predictions based on solutions
(A1) and (S4) listed in Table 22.

Table 22: The comparison of $\mathcal{B}(D_s^+ \rightarrow \bar{K}^*(892)^0 K^+)$ and $\mathcal{B}(D_s^+ \rightarrow \phi(1020) \pi^+)$ between this analysis and some theory predictions. $\mathcal{B}(exp)$ is the corresponding result of this analysis. $\mathcal{B}(A1)$, $\mathcal{B}(S4)$, $\mathcal{B}(pole)$ and $\mathcal{B}(FAT[mix])$ are theory predictions [5].

Mode	$\mathcal{B}(exp)$ (%)	$\mathcal{B}(A1)$ (%)	$\mathcal{B}(S4)$ (%)	$\mathcal{B}(pole)$ (%)	$\mathcal{B}(FAT[mix])$ (%)
$D_s^+ \rightarrow \bar{K}^*(892)^0 K^+$	3.94 ± 0.12	3.92 ± 1.13	3.93 ± 1.10	4.2 ± 1.7	4.07
$D_s^+ \rightarrow \phi(1020) \pi^+$	4.60 ± 0.17	4.49 ± 0.40	4.51 ± 0.43	4.3 ± 0.6	3.4

References

- [1] Yu Lu and Liaoyuan Dong, BESIII DocDB 682-v7.
- [2] B. Aubert *et al.* (BABAR Collaboration), Phys. Rev. D **74**, 032003 (2006).
- [3] M. Ablikim *et al.* (BES2 Collaboration), Phys. Rev. D **72**, 092002 (2005).
- [4] V. V. Anisovich *et al.*, PAN **65** 1545 (2002).
- [5] H. Y. Cheng, C. W. Chiang and A. L. Kuo, Phys. Rev. D **93**, 114010 (2016).
- [6] P. L. Frabetti *et al.* (E687 Collaboration), Phys. Lett. B **351**, 591 (1995).
- [7] R. E. Mitchell *et al.* (CLEO Collaboration), Phys. Rev. D **79**, 072008 (2009).
- [8] P. del Amo Sanchez *et al.* (BARBAR Collaboration), Phys. Rev. D **83**, 052001 (2011).
- [9] D. Cronin-Hennessy *et al.* (CLEO Collaboration), Phys. Rev. D **80**, 072001 (2009).
- [10] Andy Julin, Hajime Muramatsu and Ron Poling, BESIII DocDB 580-v1.
- [11] K. A. Olive *et al.* (Particle Data Group), Chin. Phys. C **40**, 100001 (2016)
- [12] S. U. Chung, Phys. Rev. D **56**, 7299 (1997).
- [13] <https://indico.ihep.ac.cn/event/8006/contribution/1/material/slides/0.pdf>
- [14] <https://indico.ihep.ac.cn/event/8023/contribution/1/material/slides/0.pdf>
- [15] Sifan Zhang and Hailong Ma, BESIII DocDB 630-v35.
- [16] Yu Lu and Liaoyuan Dong, BESIII DocDB 416-v30.
- [17] B. S. Zou and D. V. Bugg, Eur. Phys. J. A **16**, 537 (2003).
- [18] M. Alblikim *et al.* (BESIII Collaboration), Phys. Lett. B **607** 243 (2005).
- [19] G. Bonvicini *et al.* (CLEO Collaboration), Phys. Rev. D **78**, 052001 (2001).
- [20] M. Alblikim *et al.* (BESIII Collaboration), Phys. Rev. D **95** 072001 (2017).
- [21] Yu Lu and Liaoyuan Dong, BESIII DocDB 613-v16.
- [22] P. U. E. Onyisi *et al.* (CLEO Collaboration), Phys. Rev. D **88**, 032009 (2013).

- 2 [23] A. Zupanc *et. al.* (BELLE Collaboration), JHEP **1309**, 139 (2013).
- 3 [24] P. del Amo Sanchez *et. al.* (BABAR Collaboration), Phys. Rev. D **82**, 091003 (2010).
- 4 [25] M. Ablikim *et. al.* (BESIII Collaboration), Phys. Rev. D **95**, 032002 (2017).
- 1 [26] M. Ablikim *et. al.* (BES Collaboration), Phys. Lett. B **607**, 243 (2005).

Appendices

A The attempt to distinguish $a_0(980)$ and $f_0(980)$

Before we extract the S wave shape in the low K^+K^- mass region to describe S(980), we have attempted to distinguish $a_0(980)$ and $f_0(980)$ in amplitude analysis part. For $a_0(980)$, it is parameterized as Flatte formula,

$$P_{a_0(980)} = \frac{1}{M^2 - s - i(g_{\eta\pi}^2 \rho_{\eta\pi} + g_{K\bar{K}}^2 \rho_{K\bar{K}})}, \quad (32)$$

where $\rho_{\eta\pi}$ and $\rho_{K\bar{K}}$ are the phase space factors: $2q/\sqrt{s_a}$. We use the coupling constants $g_{\eta\pi}^2 = 0.341 \pm 0.004 \text{ GeV}^2/c^4$ and $g_{K\bar{K}}^2 = (0.892 \pm 0.022)g_{\eta\pi}^2$, reported in Ref. [25]. For $f_0(980)$, the Flatte formula used is :

$$P_{f_0(980)} = \frac{1}{M^2 - s - i(g_{\pi\pi}^2 \rho_{\pi\pi} + g_{K\bar{K}}^2 \rho_{K\bar{K}})}, \quad (33)$$

where the coupling constants $g_{\pi\pi}^2 = 0.165 \pm 0.018 \text{ GeV}^2/c^4$ and $g_{K\bar{K}}^2 = (4.21 \pm 0.33)g_{\pi\pi}^2$ are reported in Ref. [26]. We find some of the correlation coefficients of parameters in the fit of amplitude analysis are very large and we cannot measure $a_0(980)$ and $f_0(980)$ very well, which is the key motivation to extract the S wave shape. The magnitudes, phases, and fit fractions for the amplitudes are listed in Table 23. From Table 23, we can see that the error of the fit fraction of $D_s^+ \rightarrow f_0(980)\pi^+/a_0(980)\pi^+$ is very large,

Table 23: The magnitudes, phases and fit fractions (statistical errors only) for the amplitudes. $\rho_{a_0(980)}$, $\rho_{f_0(980)}/\rho_{a_0(980)}$, $\phi_{a_0(980)}$ and $\Delta\phi$ are the magnitude of $D_s^+ \rightarrow a_0(980)\pi^+$, the relative magnitude of $D_s^+ \rightarrow f_0(980)\pi^+/a_0(980)\pi^+$, the phase of $D_s^+ \rightarrow a_0(980)\pi^+$ and the relative phase of $D_s^+ \rightarrow f_0(980)\pi^+/a_0(980)\pi^+$, respectively.

Amplitude	Magnitude	Phase	Fit fractions(%)
$D_s^+ \rightarrow \bar{K}^*(892)^0 K^+$	1.0(fixed)	0.0(fixed)	47.3 \pm 3.2
$D_s^+ \rightarrow \phi(1020)\pi^+$	1.11 \pm 0.02	5.85 \pm 0.07	41.7 \pm 2.4
$D_s^+ \rightarrow a_0(980)\pi^+$	$\rho_{a_0(980)}=4.26\pm 1.92$	$\phi_{a_0(980)}=3.73\pm 0.32$	15.7 \pm 8.9
$D_s^+ \rightarrow f_0(980)\pi^+$	$\rho_{f_0(980)}/\rho_{a_0(980)}=1.06\pm 0.36$	$\Delta\phi=3.89\pm 0.35$	
$D_s^+ \rightarrow \bar{K}_0^*(1430)^0 K^+$	2.00 \pm 0.17	3.01 \pm 0.15	7.4 \pm 1.2
$D_s^+ \rightarrow f_0(1710)\pi^+$	0.78 \pm 0.09	1.13 \pm 0.14	1.8 \pm 0.5
$D_s^+ \rightarrow f_0(1370)\pi^+$	0.67 \pm 0.15	0.81 \pm 0.22	1.7 \pm 0.8

which is unacceptable.

In addition, we also have tried to fix the ratio of $D_s^+ \rightarrow f_0(980)\pi^+$ and $D_s^+ \rightarrow a_0(980)\pi^+$. However, as is discussed in the introduction part 1.1, we give up the attempt, too.